minerals

MDPI

Article

Constraints on the Formation of the Shiwu Porphyry Cu–Au Deposit in West Junggar, NW China: Insights from Tourmaline-Rich Igneous Rocks

Chu Wu [1], Chengxi Wang [1,*], Tao Hong [2,3,*], Xingwang Xu [4,5,6], Xiao Zheng [1], Wanjuan Liang [1], Kefeng Sun [1], Huijun Zhang [1], Lianhui Dong [1,4,7] and Bin Wang [1]

1 Development and Research Center of China Geology Survey, Beijing 100037, China; wuchu@mail.cgs.gov.cn (C.W.); zxiao@mail.cgs.gov.cn (X.Z.); lwanjuan@mail.cgs.gov.cn (W.L.); skefeng@mail.cgs.gov.cn (K.S.); zhuijun@mail.cgs.gov.cn (H.Z.); tjdlh@263.net (L.D.); wangbincgs@mail.cgs.gov.cn (B.W.)
2 Guangdong Provincial Key Lab of Geodynamics and Geohazards, School of Earth Sciences and Engineering, Sun Yat-sen University, Guangzhou 510275, China
3 Southern Marine Science and Engineering Guangdong Laboratory (Zhuhai), Zhuhai 519082, China
4 Key Laboratory of Mineral Resources, Institute of Geology and Geophysics, Chinese Academy of Sciences, Beijing 100029, China; xuxw@mail.iggcas.ac.cn
5 University of Chinese Academy of Sciences, Beijing 100049, China
6 Institutions of Earth Science, Chinese Academy of Sciences, Beijing 100029, China
7 Xinjiang Bureau of Geology and Mineral Resources, Urumqi 830000, China
* Correspondence: wchengxi@mail.cgs.gov.cn (C.W.); hongt5@mail.sysu.edu.cn (T.H.)

Abstract: Tourmaline tends to occur in porphyry Cu–Au deposits as an alteration or gangue mineral. However, abundant primary tourmalines in miarolitic cavities or interstitially distributed with other silicate minerals have been found in the Shiwu porphyry Cu–Au deposit in West Junggar, NW China. These tourmalines are normally accompanied by pyrite and have a high affinity for Cu and Au mineralization. A combined study of the petrology, geochronology, isotope, and mineral geochemistry data of the tourmaline-rich igneous rocks and the wallrock of tourmaline-poor pyroxene diorite has been completed. The laser ablation inductively coupled plasma mass spectrometry (LA–ICP–MS) U–Pb dating of zircons from tourmaline-poor pyroxene diorite, tourmaline-rich diorite, and tourmaline-rich andesite shows the ages of the zircons to be 317.0 ± 1.0 Ma (MSWD = 0.37, n = 18), 315.8 ± 1.0 Ma (MSWD = 0.84, n = 22), and 306.4 ± 1.6 Ma (MSWD = 1.15, n = 15), respectively. The relatively low values of Hf isotopes ($\varepsilon_{Hf}(t)$ = +6.0 to +13.6) suggest that the tourmaline-poor pyroxene diorite is sourced from a mixed melt of juvenile mantle materials with old crustal components. The tourmaline-rich diorite and the tourmaline-rich andesite that contain higher $\varepsilon_{Hf}(t)$ values (ranging from +13.3 to +17.9) are mainly derived from juvenile mantle materials. In addition, the $\varepsilon_{Hf}(t)$ values in the tourmaline-poor pyroxene diorite and the tourmaline-rich diorite (+13.3 to +16.1) and andesite (+16.3 to +17.9) are gradually rising with their age evolution, which indicates that more and more mantle-derived components are joining in their formation process. This process has also been recorded in primary tourmaline growth, e.g., the EPMA profile reveals an increase in the contents of Fe and other metals and a decrease in Al contents from the inside (core) to the outside (growth zoning). Therefore, the injection of mantle-derived magma that could supply the large amount of copper and gold was critical for the formation of the Shiwu porphyry Cu–Au deposit.

Keywords: tourmaline; mineralization; petrogenesis; Shiwu porphyry Cu–Au deposit

check for updates

Citation: Wu, C.; Wang, C.; Hong, T.; Xu, X.; Zheng, X.; Liang, W.; Sun, K.; Zhang, H.; Dong, L.; Wang, B. Constraints on the Formation of the Shiwu Porphyry Cu–Au Deposit in West Junggar, NW China: Insights from Tourmaline-Rich Igneous Rocks. *Minerals* **2023**, *13*, 612. https://doi.org/10.3390/min13050612

Academic Editor: Massimo D'Antonio

Received: 21 March 2023
Revised: 24 April 2023
Accepted: 26 April 2023
Published: 28 April 2023

Copyright: © 2023 by the authors. Licensee MDPI, Basel, Switzerland. This article is an open access article distributed under the terms and conditions of the Creative Commons Attribution (CC BY) license (https://creativecommons.org/licenses/by/4.0/).

1. Introduction

Porphyry deposits supply the most economically important class of Cu, Mo, Au, W, and Sn mineral resources [1,2]. It is widely accepted that the porphyry deposits formed in intermediate-felsic porphyritic intrusions are associated with magmatic–hydrothermal

systems. They normally contain disseminated, vein-, stockwork-, and breccia-hosted mineralization [3,4]. Tourmaline is a complex borosilicate mineral that is widely distributed in porphyry deposits and is supposed to be a key prospecting guide, especially in porphyry W and Sn deposits [5–9]. However, it is normally present as an alteration or gangue mineral in porphyry Cu, Mo, and Au deposits, e.g., Peschanka and Ol'khovka porphyry Cu deposits in Chukchi Peninsula [10]; the Aktogai porphyry Cu deposit in Kazakhstan [7]; the Agua Rica porphyry Cu–Mo–Au deposit in Argentina [11]; the Salikvan porphyry Cu–Mo deposit in northeastern Turkey [12]; the Kışladağ porphyry Au deposit in western Turkey [13]; the Coxheath porphyry Cu–Mo–Au deposit in Nova Scotia [6]; and the Shiwu porphyry Cu–Au deposit in West Junggar [14]. Few studies have revealed the primary tourmaline and its relationship with the Cu, Mo, and Au mineralization in the porphyry ore-forming system.

Previous studies have reported that the tourmaline that occurred in the Shiwu porphyry Cu–Au deposit as an alteration mineral has a crucial relationship with copper and gold mineralization [14,15].

Recently, plenty of diorites and andesites with primary tourmalines have been identified and sampled in the Shiwu porphyry Cu–Au deposit. These tourmalines normally intergrow with pyrite, and their assemblages fill into miarolitic cavities or are interstitially distributed with other silicate minerals, especially augen quartz phenocrysts. The sulfide-tourmaline-rich diorites and andesites may constrain Cu and Au mineralization in the Shiwu porphyry Cu–Au deposit. Therefore, our work focuses on both the sulfide-tourmaline-rich igneous rocks and the main wallrock of pyroxene diorite along with the previously documented intrusions at Shiwu. We integrate our field observations with petrography, geochronology, and mineral geochemistry and combine these with the previous database of intrusions in order to (1) define the petrogenesis of sulfide-tourmaline-rich igneous rocks and (2) ascertain the origin and evolution of copper and gold in the Shiwu porphyry Cu–Au deposit.

2. Geological Background

2.1. Regional Geological Setting

The West Junggar is located in the Central Asian Orogenic Belt which has occupied the core area of its west domain (CAOB, Figure 1a) [16,17]. It can be subdivided into the Laba-Junggar terrane, the Baogutu arc, the Barluk–Mayile–Tangbale–Darbut (BMTD) ophiolite belt, the Barluk continental arc (CA), the Xiemisitai oceanic island arc (OIA), and the Sawuer OIA from south to north (Figure 1b) [18]. The southeastern Laba–Junggar terrane has been almost covered by Paleozoic–Mesozoic–Cenozoic sediments. However, the recent discovery of Precambrian zircons and a continent-like thick crust suggest that it could be a microcontinent [19]. The Late Paleozoic Baogutu arc contains numerous Precambrian zircons, which has been considered as a western marginal fragment of the Laba–Junggar terrane due to the eastward subduction of the Junggar Oceanic plate [19,20]. The immense central area mainly consists of the Mayile ophiolite, the Tangbale ophiolite, the Barluk ophiolite, the Darbut ophiolite, and the Karamay ophiolite (BMTD ophiolite belt) [17,18]. It is likely to be the residue Junggar oceanic plate that has been unconformably covered by Late Carboniferous–Permian sedimentary and volcaniclastic sequences and intruded by Late Carboniferous diorite–granite plutons [17,18,20–22]. The Sawuer and Xiemisitai arcs, characterized by the outcrops of abundant Early Paleozoic adakites, porphyry deposits, and calc-alkaline granites, have been identified as oceanic island arcs in the Paleo-Asian ocean [4,17,21].

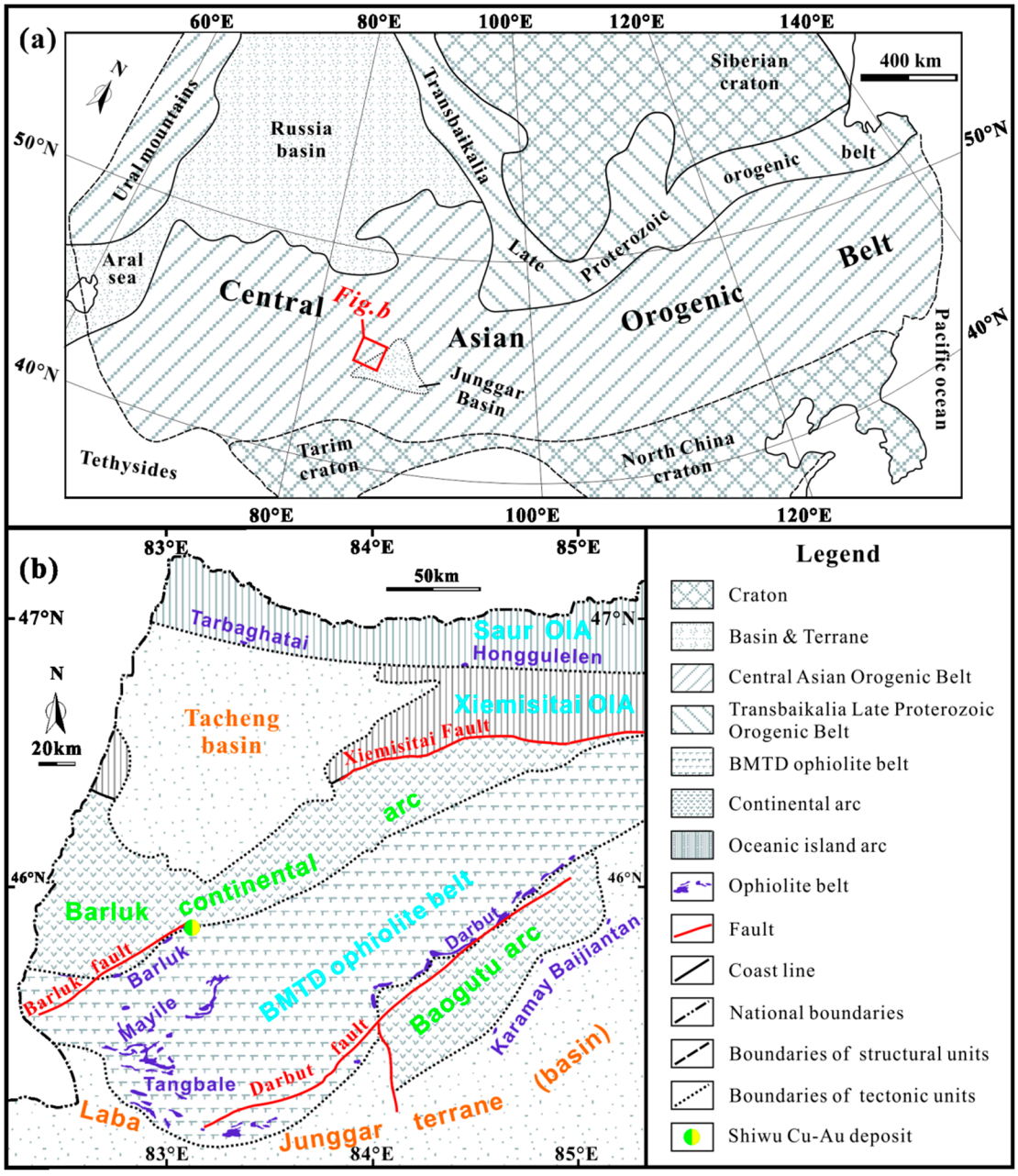

Figure 1. Location ((**a**), revised from [16,23]) and tectonic units ((**b**), revised from [18,20]) of the West Junggar, CAOB. Abbreviation: BMTD: Barluk–Mayile–Tangbale–Darbut; OIA: oceanic island arc.

Located between the Kazakhstan Continent and the BMTD ophiolite belt is the Barluk arc, bound by the Barluk ophiolite belt on the southeast and the Tacheng basin on the northwest (Figure 1b) [18,20,23]. The Early Paleozoic (ca. 509–492 Ma) Barluk ophiolite belt mainly consists of wehrlite clinopyrixene peridotite, cumulated gabbro, pillow lava and chert and minor metamorphic blocks has been defined as the northwestern margin of the Junggar oceanic plate [24–27]. There is a general recognition that the Barluk arc is a Late Paleozoic (ca. 408–259 Ma) island arc [26,28] or continental arc [18] which has been produced by the northwestward subduction of the Junggar oceanic plate. The majority in this area is composed of Devonian–Carboniferous sedimentary and volcaniclastic sequences, e.g., sandstone, mudstone, tuff, tuffaceous sandstone, tuffaceous siltstone, lava, and volcanic breccia [18,27,29]. These Devonian–Carboniferous sedimentary and volcaniclastic sequences have been intruded by Late Carboniferous–Permian dioritic-granitic intrusions (e.g., plutons, stocks or porphyries), e.g., the 324–302 Ma Shiwu porphyries [18,28,30], the

325–259 Ma North Barleik stocks [29,31], the 313–310 Ma Jiamantielieketi plutons [26,32], the 277 Ma Tasiti pluton [26], and the 298–294 Ma Suyunhe porphyries [33].

2.2. Deposit Geological Setting

The Shiwu porphyry Cu–Au deposit is situated in the southeast in the Barluk arc (Figure 1b). Its plutons composed of granitic porphyry, diorite, pyroxene diorite, and gabbro (Figure 2) are present in the Middle Devonian Barluk Formation (D_2b), composed of debris tuff, tuff, and tuffaceous siltstone [18]. The outcrops of granitic porphyry, which have no apparent contact with other intrusions, are located in the northern Shiwu area and characterized by rare alteration and mineralization. However, sulfides rich in Cu–Au occur in the tourmaline veins, networks of tourmaline (-quartz) veinlets, tourmaline matrix in brecciated wallrock, and tourmaline disseminated in altered wallrock [34]. Hosted by a ca. 3 km^2 shallow gabbroic–dioritic complex, the deposit is present in the northwestern part of the Shiwu intrusive complex (Figure 2). The pyroxene diorite forms the most widely distributed intrusions in the Shiwu porphyry Cu–Au deposit. Most of the pyroxene diorite is present in irregular–shape plutons or dikes, whilst some of the gabbro dikes are embedded within the pyroxene diorite itself. There are some small dioritic porphyry bodies that occur close to or within the pyroxene diorite pluton. Moreover, some intermediate–acidic volcanic lavas, e.g., rhyolite, dacite, and andesite, are overlaying the Barluk Formation (D_2b) along a mountain front. Detailed petrologic diagnoses of these igneous rocks in the Shiwu porphyry Cu–Au deposit have been introduced by Li et al. [28] and Wu et al. [18].

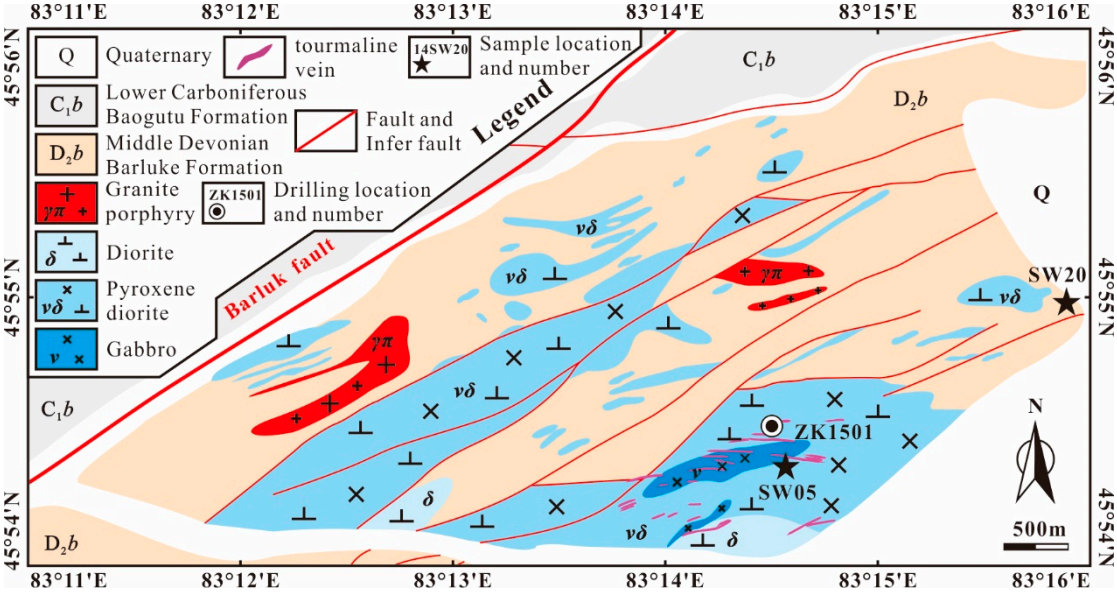

Figure 2. Geological map of Shiwu deposit (modified after [18]).

2.2.1. Tourmaline-Rich Igneous Rocks

In this study, the tourmaline-rich diorite and andesite are newly identified igneous rocks in the Shiwu porphyry Cu–Au deposit that have a prominent affinity to Cu–Au mineralization. Tourmaline-rich diorite occurs as blocks or veins within the pyroxene diorite pluton (Figure 3a,b), whereas tourmaline-rich andesite is distributed in the Middle Devonian Barluk Formation (D_2b) as dikes and present in tourmaline breccia as residual blocks or clasts (Figure 3c). Their detailed petrographic descriptions are provided as follows:

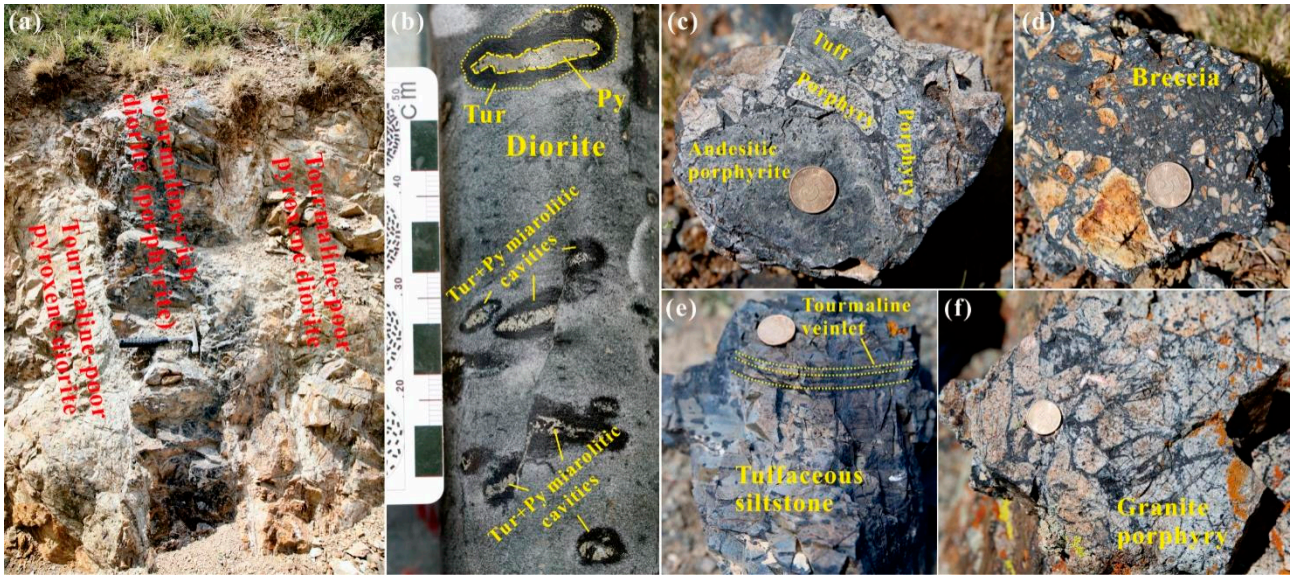

Figure 3. Representative photographs of tourmaline-rich igneous rocks. Outcrop photographs showing tourmaline-rich diorite (porphyrite) intruding into the tourmaline-poor pyroxene diorite (**a**); Hand specimen of diorite with pyrite-tourmaline miarolitic cavities (**b**); Tourmaline breccia with clasts of tuff, porphyry, and andesite (**c**); Tourmaline breccia with inclusions of felsic minerals (**d**); Tourmaline veinlets intruding into the tuffaceous siltstone (**e**) and granite porphyry (**f**). Abbreviation: Py: pyrite; Tur: tourmaline.

The gray-green tourmaline-rich diorite occurs as irregular–shape plutons or dikes that have a mineral composition of fine-grained 20 to 80 μm plagioclase (50–55 vol%), 20 to 60 μm hornblende (8–12 vol%), 30 to 50 μm biotite (8–12 vol%), 20 to 300 μm tourmaline (8–10 vol%), and 20 to 50 μm quartz (5–8 vol%). The accessory minerals consist of apatite, zircon, ilmenite, magnetite, pyrite, and chalcopyrite. Most mineral phenocrysts are hypidiomorphic granular. The tourmaline and pyrite aggregates in the tourmaline-rich diorite are round or elliptical and 10–50 mm in length, with elongation ratios from 1 to 4. They have a miarolitic-like texture with a tourmaline and pyrite intergrowth halo and a pyrite core (Figure 4a,b).

The dark-green tourmaline-rich andesite is mainly composed of aggregates of idiomorphic to hypidiomorphic tourmaline and pyrite (15–25 vol%, 2–20 mm), augen phenocrysts of idiomorphic quartz (15–20 vol%, 20–300 μm), a matrix of heteromorphic felsic minerals (e.g., plagioclase, quartz, and biotite), and minor accessory minerals (e.g., apatite, zircon, ilmenite, magnetite, and pyrite). It is characterized by a porphyritic texture. The tourmaline and pyrite in the tourmaline-rich andesite occur as an irregular–shape aggregates. Tourmaline also occurs as brown, black, and dark-green isolated needles up to 10 mm long or as radiated aggregates of needles (Figure 4c,d). Pyrite is present as idiomorphic grains (5–15 μm) with a dark metal color.

Moreover, plenty of volcanic breccias located in the northeast of the Shiwu porphyry Cu–Au deposit (Figure 2) contain tuff, porphyry, andesite, and felsic minerals (Figure 3c,d). The cement is mainly atrovirens or black tourmaline (Figure 3c,d) [28]. Tourmaline intrudes into the wallrock of tuffaceous siltstone and granite porphyry as veinlets (Figure 3e,f).

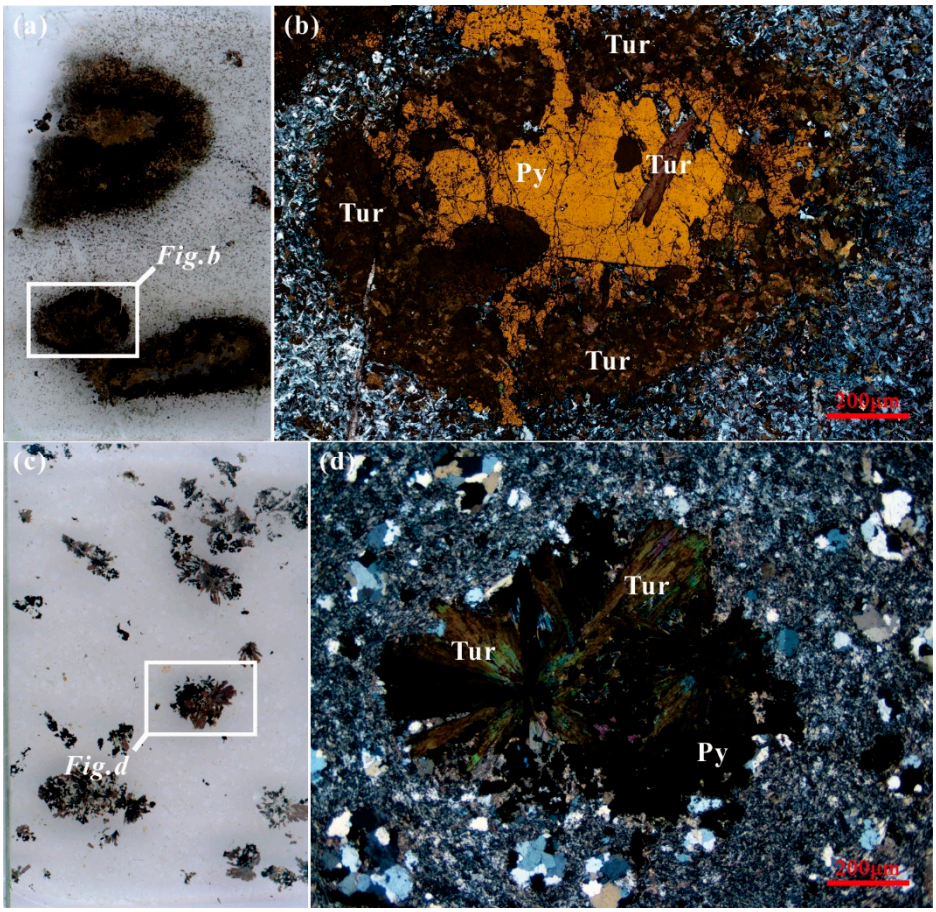

Figure 4. The scanning image (**a**) with an enlarged polarized microscopic image (**b**) showing pyrite-tourmaline miarolitic cavities in tourmaline-rich diorite. The scanning image (**c**) with an enlarged polarized microscopic image (**d**) showing augen tourmaline with pyrite and augen quartz crystals in tourmaline-rich andesite. Abbreviation: Py: pyrite; Tur: tourmaline.

2.2.2. Alteration and Mineralization

Based on field and microscopic observations, typical hydrothermal alterations, including potassic, Ca–Na silicate, tourmaline, propylitic, phyllic, and calcic zones, have been identified in igneous rocks [14]. In particular, the Cu–Au mineralization is intimately related to tourmaline alteration [14,18,28]. Potassic and Ca–Na silicate alterations occurred prior to mineralization and were characterized by secondary biotite + K-feldspar + actinolite + albite + magnetite ± epidote alterations, mainly in the diorite and pyroxene diorite. The tourmaline alteration together with simultaneous or subsequent propylitic and phyllic alterations are widely distributed in the entire Shiwu intrusive complex. They exhibit a tourmaline + epidote + chlorite + sericite + quartz + carbonate + pyrite assemblage that normally overprints the precursor potassic and Ca–Na silicate alterations and an affinity to the main mineralization. Moreover, the late calcilization exhibited by calcite + chlorite has no affinity to mineralization [14,28,34].

The Shiwu porphyry Cu–Au deposit contains 2×10^4 t of Cu with average grades of 0.3–0.5 wt% and 1.2 t of Au averaging 1.2–5.5 g/t, predominately as disseminated mineralization with minor amounts of vein-type and breccia-hosted mineralization [34]. Chalcopyrite, pyrite, and gold are main ore minerals accompanied by subordinate molybdenite, arsenopyrite, bornite, galena, sphalerite, ilmenite, and titanomagnetite. The gangue minerals are primarily composed of biotite, K-feldspar, tourmaline, sericite, amphibole, epidote, chlorite, calcite, and quartz [14,28,34]. The Au mineralization is concentrated (>2 g/t) in the recently identified tourmaline-bearing igneous rocks, but is absent in other intrusions [34].

3. Sample Selection and Analytical Technique

In this paper, after a detailed petrographic examination for zircon U–Pb dating by laser ablation inductively coupled plasma mass spectrometry (LA–ICP–MS), tourmaline-poor pyroxene diorite sample SW05, tourmaline-rich diorite sample ZK1501-480, and tourmaline-rich andesite sample SW20 were selected from the Shiwu deposit.

For zircon separation, conventional heavy fraction and magnetic separation techniques were used. The freshest unbroken representative zircon grains were collected and mounted in epoxy resin mounts. Transmitted and reflected light photomicrographs and cathodoluminescence (CL) images revealed the morphology, the internal structure, the pellucidity, the inclusion, and the zonation. Before CL imaging and LA–ICP–MS analysis, all the epoxy resin mounts with zircon grains were polished to expose half-sections and vacuum-coated with high-purity gold. An Agilent 7500a Q–ICP–MS with a 193 nm excimer laser ablation system was devoted to detecting high-quality U, Th, and Pb isotopic contents of zircon grains. Zircon 91500 and GJ-1 were used as the standards for U–Pb dating, and silicate glass NIST 610 was used as the reference material. The spot diameter, laser frequency, and laser energy were 45 μm, 6 Hz, and 25 J/cm^2, respectively. Xie et al. [35] provided detailed operating and data processing procedures. Common Pb corrections and reductions were made using the method described by Anderson [36] and the Isoplot/Ex version 2.49 programs of Ludwig [37]. Table 1 presents all the zircon U–Pb data.

Corresponding to geochronological analysis, partially U–Pb dating analyzed zircon grains from the tourmaline-poor pyroxene diorite (sample SW05), the tourmaline-rich diorite (sample ZK1501-480), and the tourmaline-rich andesite (sample SW20) were employed for Lu–Hf isotopic test. A Neptune MC–ICP–MS with an ArF excimer laser ablation system was used to obtain high-precision Lu and Hf isotopes. The diameter of ablation pit, the repetition rate of laser, and the energy of laser were 45 μm, 8 Hz, and 15 J/cm^2, respectively. Wu et al. [38] described the detailed analytical procedures. Zircon 91500 was used to monitor the instrument status and yielded $^{176}Hf/^{177}Hf$ ratio of 0.282288 ± 15 (2σ) and $^{176}Lu/^{177}Hf$ ratio of 0.00031. It is consistent with the commonly accepted $^{176}Hf/^{177}Hf$ ratio of 0.282284 ± 3 (1σ) measured using the solution method [39,40]. The initial $_{\varepsilon Hf}(t)$ values and the corresponding depleted mantle model ages {T_{DM}(Hf)} were calculated at their corresponding zircon $^{206}Pb/^{238}U$ ages. Table 2 summarizes the detailed zircon Lu–Hf isotopic data.

To ascertain the mineral chemistry of tourmaline, electron probe microanalysis (EPMA) was performed using a JXA-8100 electron microprobe operated in wavelength dispersive spectrometer (WDS) mode to examine thin sections of the tourmaline-rich diorite (sample ZK1501-480) and the tourmaline-rich andesite (sample SW20). The beam diameter, the accelerating voltage, and the sample current were 3 μm, 15 kV, and 10 nA, respectively. The counting times for all elements were 20 s. Well-defined natural minerals (such as silicates, oxides, sulfides, salts, and pure elements) were employed as standards. The atomic number–absorption–fluorescence (ZAF) procedure was used for correcting all the analytical data. Moreover, the major element contents in this study were all converted into atoms per formula unit as well [41,42]. Table 3 exhibits the final EPMA results.

Table 1. LA–ICP–MS zircon U–Pb ages of tourmaline-related igneous rocks in the Shiwu Cu–Au deposit, West Junggar.

Plot No.	Content/10^{-6}			Th/U	$^{207}Pb/^{206}Pb$		$^{207}Pb/^{235}U$		$^{206}Pb/^{238}U$		$^{207}Pb/^{206}Pb$		$^{207}Pb/^{235}U$		$^{206}Pb/^{238}U$	
	Pb	Th	U		Ratio	±σ	Ratio	±σ	Ratio	±σ	Age/Ma	±σ	Age/Ma	±σ	Age/Ma	±σ
SW05, tourmaline-poor pyroxene diorite																
1	8.4	88	139	0.6	0.0527	0.0021	0.3674	0.0134	0.0506	0.0009	315	51	318	10	318	6
2	14.6	169	216	0.8	0.0530	0.0020	0.3709	0.0138	0.0508	0.0007	328	59	320	10	319	4
3	9.3	69	158	0.4	0.0528	0.0017	0.3680	0.0109	0.0506	0.0008	318	39	318	8	318	5
4	10.5	102	173	0.6	0.0529	0.0021	0.3661	0.0134	0.0502	0.0010	325	48	317	10	315	6
5	12.7	150	202	0.7	0.0528	0.0021	0.3674	0.0140	0.0505	0.0007	318	60	318	10	317	4
6	8.2	63	140	0.5	0.0528	0.0016	0.3664	0.0101	0.0504	0.0008	318	33	317	7	317	5
7	13.0	124	204	0.6	0.0527	0.0019	0.3655	0.0121	0.0503	0.0009	317	43	316	9	316	6
8	10.1	117	163	0.7	0.0528	0.0017	0.3676	0.0108	0.0505	0.0009	321	37	318	8	317	5
9	7.4	63	127	0.5	0.0527	0.0021	0.3644	0.0134	0.0502	0.0009	315	50	316	10	316	6
10	9.5	85	163	0.5	0.0528	0.0019	0.3680	0.0120	0.0505	0.0008	321	44	318	9	318	5
11	7.8	77	134	0.6	0.0526	0.0028	0.3657	0.0175	0.0504	0.0013	310	65	316	13	317	8
12	10.5	106	180	0.6	0.0525	0.0015	0.3584	0.0093	0.0495	0.0008	307	32	311	7	312	5
13	18.3	174	316	0.6	0.0527	0.0025	0.3667	0.0160	0.0505	0.0012	315	59	317	12	318	7
14	8.9	89	153	0.6	0.0529	0.0021	0.3659	0.0130	0.0502	0.0010	322	46	317	10	316	6
15	12.3	94	211	0.4	0.0527	0.0014	0.3650	0.0090	0.0503	0.0008	314	30	316	7	316	5
16	14.5	164	229	0.7	0.0528	0.0014	0.3674	0.0087	0.0505	0.0007	318	30	318	6	318	4
17	7.7	77	133	0.6	0.0528	0.0022	0.3669	0.0142	0.0504	0.0010	319	53	317	11	317	6
18	9.4	90	153	0.6	0.0528	0.0016	0.3678	0.0101	0.0505	0.0008	321	35	318	7	318	5
ZK1501-480, tourmaline-rich diorite																
1	7.7	79	126	0.6	0.0527	0.0024	0.3645	0.0153	0.0502	0.0009	314	62	316	11	316	6
2	6.7	50	113	0.4	0.0533	0.0041	0.3747	0.0275	0.0510	0.0012	342	126	323	20	320	7
3	21.9	70	403	0.2	0.0527	0.0013	0.3644	0.0085	0.0501	0.0006	318	31	316	6	315	4
4	4.9	22	89	0.2	0.0527	0.0033	0.3646	0.0214	0.0502	0.0012	317	91	316	16	316	7
5	10.1	53	179	0.3	0.0527	0.0020	0.3651	0.0131	0.0502	0.0008	317	53	316	10	316	5
6	9.4	60	167	0.4	0.0528	0.0024	0.3666	0.0150	0.0504	0.0010	320	56	317	11	317	6
7	10.3	98	172	0.6	0.0528	0.0025	0.3633	0.0153	0.0499	0.0011	318	56	315	11	314	7
8	7.0	27	126	0.2	0.0528	0.0020	0.3664	0.0130	0.0504	0.0009	319	48	317	10	317	6
9	3.8	36	63	0.6	0.0528	0.0030	0.3657	0.0194	0.0503	0.0012	318	78	316	14	316	7
10	7.8	62	134	0.5	0.0529	0.0021	0.3698	0.0134	0.0507	0.0009	325	51	319	10	319	5
11	9.7	54	170	0.3	0.0527	0.0036	0.3643	0.0237	0.0502	0.0012	315	105	315	18	315	7
12	6.0	32	106	0.3	0.0528	0.0033	0.3668	0.0209	0.0504	0.0015	321	78	317	16	317	9

Table 1. *Cont.*

Plot No.	Content/10^{-6}			Th/U	$^{207}Pb/^{206}Pb$		$^{207}Pb/^{235}U$		$^{206}Pb/^{238}U$		$^{207}Pb/^{206}Pb$		$^{207}Pb/^{235}U$		$^{206}Pb/^{238}U$	
	Pb	Th	U		Ratio	±σ	Ratio	±σ	Ratio	±σ	Age/Ma	±σ	Age/Ma	±σ	Age/Ma	±σ
13	7.3	63	123	0.5	0.0528	0.0030	0.3711	0.0193	0.0510	0.0013	320	73	320	14	321	8
14	5.3	48	88	0.5	0.0528	0.0048	0.3689	0.0327	0.0507	0.0012	318	159	319	24	319	7
15	6.5	33	113	0.3	0.0535	0.0055	0.3665	0.0365	0.0497	0.0014	348	175	317	27	313	8
16	7.5	43	132	0.3	0.0525	0.0019	0.3581	0.0116	0.0495	0.0009	308	41	311	9	311	6
17	8.1	70	139	0.5	0.0527	0.0022	0.3633	0.0141	0.0500	0.0010	315	52	315	11	315	6
18	3.2	25	53	0.5	0.0529	0.0033	0.3707	0.0216	0.0509	0.0013	324	85	320	16	320	8
19	9.4	59	165	0.4	0.0526	0.0018	0.3573	0.0110	0.0493	0.0008	311	40	310	8	310	5
20	13.2	77	231	0.3	0.0527	0.0019	0.3657	0.0119	0.0503	0.0009	317	42	316	9	316	6
21	10.8	75	183	0.4	0.0532	0.0024	0.3686	0.0156	0.0503	0.0009	337	63	319	12	316	5
22	5.0	37	84	0.4	0.0526	0.0025	0.3640	0.0153	0.0502	0.0012	312	54	315	11	316	7
SW20, tourmaline-rich andesite																
1	20.2	98	376	0.3	0.0532	0.0027	0.3551	0.0171	0.0484	0.0009	337	110	309	13	305	6
2	12.8	77	231	0.3	0.0527	0.0033	0.3585	0.0213	0.0493	0.0013	318	138	311	16	310	8
3	11.7	71	215	0.3	0.0529	0.0040	0.3491	0.0254	0.0478	0.0012	326	163	304	19	301	7
4	11.1	113	185	0.6	0.0528	0.0021	0.3590	0.0135	0.0494	0.0008	318	88	312	10	311	5
5	5.7	49	98	0.5	0.0526	0.0055	0.3534	0.0364	0.0487	0.0012	313	223	307	27	307	7
6	7.5	50	136	0.4	0.0524	0.0022	0.3502	0.0135	0.0484	0.0009	305	92	305	10	305	6
7	5.8	28	108	0.3	0.0532	0.0055	0.3569	0.0348	0.0486	0.0017	338	217	310	26	306	10
8	11.5	59	207	0.3	0.0526	0.0031	0.3602	0.0200	0.0497	0.0010	311	127	312	15	313	6
9	4.7	22	88	0.2	0.0525	0.0066	0.3470	0.0431	0.0479	0.0012	309	264	303	33	302	7
10	13.0	78	227	0.3	0.0532	0.0029	0.3668	0.0189	0.0500	0.0010	336	117	317	14	315	6
11	7.2	38	133	0.3	0.0528	0.0045	0.3510	0.0287	0.0483	0.0013	318	183	305	22	304	8
12	8.7	51	161	0.3	0.0529	0.0034	0.3536	0.0219	0.0485	0.0009	322	139	307	16	306	6
13	9.4	37	176	0.2	0.0526	0.0032	0.3515	0.0211	0.0485	0.0009	311	134	306	16	305	5
14	11.4	65	207	0.3	0.0532	0.0023	0.3551	0.0148	0.0484	0.0008	339	95	309	11	305	5
15	5.7	34	101	0.3	0.0524	0.0065	0.3490	0.0426	0.0483	0.0012	302	260	304	32	304	7

Table 2. MC–ICP–MS zircon Lu–Hf isotopic results of tourmaline-related igneous rocks in the Shiwu Cu–Au deposit, West Junggar.

Plot No. (Plot No. in Age Test)	$^{206}Pb/^{238}U$ (Ma)	$^{176}Yb/^{177}Hf$ (Corr)	2 Sigma	$^{176}Lu/^{177}Hf$ (Corr)	2 Sigma	$^{176}Hf/^{177}Hf$ (Corr)	2 Sigma	$^{176}Hf/^{177}Hf_i$	$^{176}Hf/^{177}Hf_i$ (DM)	$\varepsilon_{Hf}(0)$	$\varepsilon_{Hf}(t)$	2 Sigma	$f_{Lu/Hf}$	T_{DM1} (Hf)	$T_{DM}{}^{C}$	T_{DM2} (Hf)
SW05, tourmaline-poor pyroxene diorite																
1(1)	318	0.044586	0.000675	0.001956	0.000028	0.282957	0.000018	0.282945	0.283022	6.5	13.1	0.6	−0.94	430	493	492
2(2)	319	0.034718	0.000244	0.001589	0.000010	0.282962	0.000024	0.282953	0.283021	6.7	13.4	0.8	−0.95	418	475	474
3(5)	317	0.021978	0.000043	0.000904	0.000001	0.282965	0.000039	0.282960	0.283022	6.8	13.6	1.4	−0.97	406	460	459
4(6)	317	0.039445	0.000224	0.001517	0.000007	0.282755	0.000053	0.282746	0.283022	−0.6	6.0	1.9	−0.95	715	947	945
5(7)	316	0.029967	0.000048	0.001149	0.000004	0.282845	0.000045	0.282838	0.283023	2.6	9.3	1.6	−0.97	580	738	736
6(9)	316	0.021606	0.000042	0.000804	0.000001	0.282780	0.000044	0.282776	0.283023	0.3	7.1	1.6	−0.98	666	880	878
7(10)	318	0.039388	0.000099	0.001351	0.000003	0.282776	0.000101	0.282768	0.283022	0.1	6.8	3.6	−0.96	682	896	894
8(11)	317	0.055057	0.000160	0.001892	0.000005	0.282857	0.000053	0.282846	0.283022	3.0	9.6	1.9	−0.94	574	720	718
9(14)	316	0.039683	0.000426	0.001295	0.000015	0.282797	0.000060	0.282789	0.283023	0.9	7.6	2.1	−0.96	650	849	846
10(16)	318	0.028213	0.000123	0.000943	0.000003	0.282866	0.000055	0.282860	0.283022	3.3	10.1	1.9	−0.97	547	686	684
ZK1501-480, tourmaline-rich diorite																
1(4)	316	0.038913	0.000391	0.001678	0.000016	0.283020	0.000045	0.283010	0.283023	8.8	15.4	1.6	−0.95	335	346	346
2(7)	314	0.036240	0.000567	0.001582	0.000013	0.283006	0.000046	0.282997	0.283024	8.3	14.9	1.6	−0.95	354	377	377
3(9)	316	0.027726	0.000073	0.001367	0.000003	0.282961	0.000032	0.282953	0.283023	6.7	13.3	1.1	−0.96	417	477	476
4(11)	315	0.034192	0.000471	0.001499	0.000021	0.282972	0.000022	0.282963	0.283024	7.1	13.7	0.8	−0.95	402	454	453
5(12)	317	0.024028	0.000229	0.001114	0.000010	0.282985	0.000019	0.282978	0.283022	7.5	14.3	0.7	−0.97	380	417	417
6(13)	321	0.034208	0.000164	0.001433	0.000004	0.283027	0.000045	0.283019	0.283019	9.0	15.8	1.6	−0.96	322	322	322
7(14)	319	0.036330	0.000183	0.001526	0.000003	0.283033	0.000042	0.283024	0.283021	9.2	15.9	1.5	−0.95	314	312	312
8(15)	313	0.015792	0.000050	0.000635	0.000002	0.282993	0.000043	0.282989	0.283025	7.8	14.6	1.5	−0.98	364	396	395
9(17)	315	0.030405	0.000064	0.001184	0.000002	0.283002	0.000041	0.282995	0.283024	8.1	14.8	1.5	−0.96	356	380	380
10(19)	310	0.053167	0.000168	0.001724	0.000008	0.283045	0.000040	0.283035	0.283027	9.7	16.1	1.4	−0.95	298	292	292
SW20, tourmaline-rich andesite																
1(2)	310	0.045308	0.000026	0.001506	0.000003	0.283049	0.000042	0.283041	0.283027	9.8	16.3	1.5	−0.95	291	280	280
2(3)	301	0.049016	0.000248	0.001614	0.000006	0.283098	0.000038	0.283089	0.283034	11.5	17.8	1.4	−0.95	221	175	176
3(4)	311	0.022555	0.000032	0.000842	0.000001	0.283082	0.000045	0.283077	0.283027	11.0	17.6	1.6	−0.97	239	194	195
4(6)	305	0.033724	0.000127	0.001354	0.000007	0.283095	0.000045	0.283087	0.283031	11.4	17.9	1.6	−0.96	224	175	176
5(8)	313	0.021782	0.000124	0.000947	0.000004	0.283071	0.000046	0.283065	0.283025	10.6	17.3	1.6	−0.97	256	221	222
6(10)	315	0.035277	0.000613	0.001497	0.000023	0.283073	0.000042	0.283064	0.283024	10.6	17.2	1.5	−0.95	257	223	224
7(11)	304	0.039870	0.000675	0.001689	0.000024	0.283071	0.000062	0.283061	0.283032	10.6	16.9	2.2	−0.95	261	237	237
8(12)	306	0.032230	0.000137	0.001376	0.000006	0.283068	0.000041	0.283061	0.283030	10.5	16.9	1.4	−0.96	262	236	237
9(13)	305	0.027915	0.000499	0.001211	0.000020	0.283083	0.000044	0.283076	0.283031	11.0	17.5	1.6	−0.96	240	202	202
10(15)	304	0.039918	0.000298	0.001656	0.000014	0.283076	0.000037	0.283066	0.283032	10.7	17.1	1.3	−0.95	254	225	225

Table 3. Major elements (%) of EPMA profiles for representative tourmaline crystals from sulfide-tourmaline-rich igneous rocks in the Shiwu Cu–Au deposit, West Junggar.

Lithology	Plot Number	SiO_2	Al_2O_3	FeO	MgO	CaO	Na_2O	K_2O	TiO_2	MnO	* Li_2O	Si	Al	Fe	Mg	Ca	Na	K	Ti	Mn	* Li	X-Site Vacancy
tourmaline-rich diorite	1	35.88	29.88	12.88	4.36	1.41	1.74	0.03	0.14	0.05	0.75	6.29	6.18	1.89	1.14	0.27	0.59	0.01	0.02	0.07	0.53	0.14
	2	36.05	29.96	12.68	4.35	1.16	1.93	0.05	0.11	0.05	0.79	6.32	6.19	1.86	1.14	0.22	0.66	0.01	0.01	0.08	0.56	0.11
	3	36.26	31.32	11.50	4.58	1.42	1.56	0.02	0.23	0.05	0.85	6.36	6.48	1.69	1.20	0.27	0.53	0.00	0.03	0.08	0.60	0.20
	4	36.25	31.62	11.07	4.53	1.23	1.69	0.02	0.45	0.03	0.85	6.36	6.54	1.62	1.18	0.23	0.57	0.00	0.06	0.09	0.60	0.19
	5	36.35	32.47	10.01	4.58	1.04	1.66	0.02	0.84	0.00	0.88	6.38	6.71	1.47	1.20	0.20	0.56	0.00	0.11	0.10	0.62	0.24
	6	36.52	33.28	9.63	4.43	0.68	1.77	0.03	0.34	0.02	0.93	6.41	6.88	1.41	1.16	0.13	0.60	0.01	0.04	0.09	0.66	0.26
	7	37.22	33.51	9.26	4.55	0.51	1.92	0.04	0.14	0.00	1.13	6.53	6.93	1.36	1.19	0.10	0.65	0.01	0.02	0.09	0.80	0.24
	8	36.65	33.68	8.99	4.53	0.52	1.72	0.03	0.18	0.00	0.97	6.43	6.96	1.32	1.18	0.10	0.59	0.01	0.02	0.09	0.68	0.31
	9	35.93	33.68	9.64	4.39	1.06	1.70	0.03	0.28	0.04	0.76	6.30	6.96	1.41	1.15	0.20	0.58	0.01	0.04	0.07	0.54	0.22
	10	36.44	31.98	10.01	4.76	1.07	1.73	0.03	0.71	0.01	0.91	6.39	6.61	1.47	1.24	0.20	0.59	0.01	0.09	0.06	0.64	0.20
	11	36.31	30.68	10.91	5.00	1.40	1.75	0.08	0.62	0.02	0.87	6.37	6.34	1.60	1.31	0.26	0.60	0.02	0.08	0.10	0.61	0.12
	12	35.91	28.17	12.85	5.57	1.90	1.56	0.02	0.83	0.07	0.75	6.30	5.82	1.89	1.46	0.36	0.53	0.00	0.11	0.09	0.53	0.11
	13	36.24	27.87	13.23	5.31	1.88	1.62	0.02	0.67	0.09	0.85	6.36	5.76	1.94	1.39	0.35	0.55	0.00	0.09	0.11	0.60	0.09
tourmaline-rich andesite	1	35.67	28.46	15.68	3.82	1.65	1.73	0.11	0.03	0.03	0.69	6.26	5.88	2.30	1.00	0.31	0.59	0.02	0.00	0.06	0.48	0.08
	2	35.86	27.91	14.44	4.70	1.78	1.62	0.09	0.03	0.02	0.74	6.29	5.77	2.12	1.23	0.33	0.55	0.02	0.00	0.08	0.52	0.09
	3	36.15	28.69	12.98	5.33	1.78	1.73	0.05	0.02	0.02	0.82	6.34	5.93	1.90	1.39	0.33	0.59	0.01	0.00	0.08	0.58	0.07
	4	36.44	30.57	11.80	4.95	1.19	1.67	0.07	0.02	0.02	0.91	6.39	6.32	1.73	1.29	0.22	0.57	0.02	0.00	0.08	0.64	0.19
	5	36.43	30.41	12.00	4.84	1.03	1.83	0.06	0.00	0.03	0.90	6.39	6.29	1.76	1.27	0.19	0.62	0.01	0.00	0.08	0.64	0.17
	6	36.48	30.22	12.06	4.82	1.24	1.76	0.08	0.02	0.02	0.92	6.40	6.25	1.77	1.26	0.23	0.60	0.02	0.00	0.07	0.65	0.15
	7	36.20	29.47	13.07	4.76	1.51	1.64	0.06	0.03	0.01	0.84	6.35	6.09	1.92	1.24	0.28	0.56	0.01	0.00	0.04	0.59	0.14
	8	35.62	27.85	14.60	4.64	1.87	1.57	0.09	0.05	0.02	0.67	6.25	5.76	2.14	1.21	0.35	0.53	0.02	0.01	0.05	0.47	0.09

Note: * means Li-oxide and Li are calculated based on tourmaline chemical formula.

4. Results

4.1. Geochronology

Zircon grains from the tourmaline-poor pyroxene diorite (sample SW05), the tourmaline-rich diorite (sample ZK1501-480), and the tourmaline-rich andesite (sample SW20) display oscillatory zoning in CL images, are 100–280 μm in size, and have elongation ratios of 1.00 to 3.00. They plot on or near the Concordia line and yielded concordant $^{206}Pb/^{238}U$ of 317.0 ± 1.0 Ma (MSWD = 0.37, n = 18) for the tourmaline-poor pyroxene diorite, 315.8 ± 1.0 Ma (MSWD = 0.84, n = 22) for the tourmaline-rich diorite, and 306.4 ± 1.6 Ma (MSWD = 1.15, n = 15) for the tourmaline-rich andesite (Figure 5). The zircons have Th/U ratios of 0.2 to 0.8, similar to magmatic zircons [43,44].

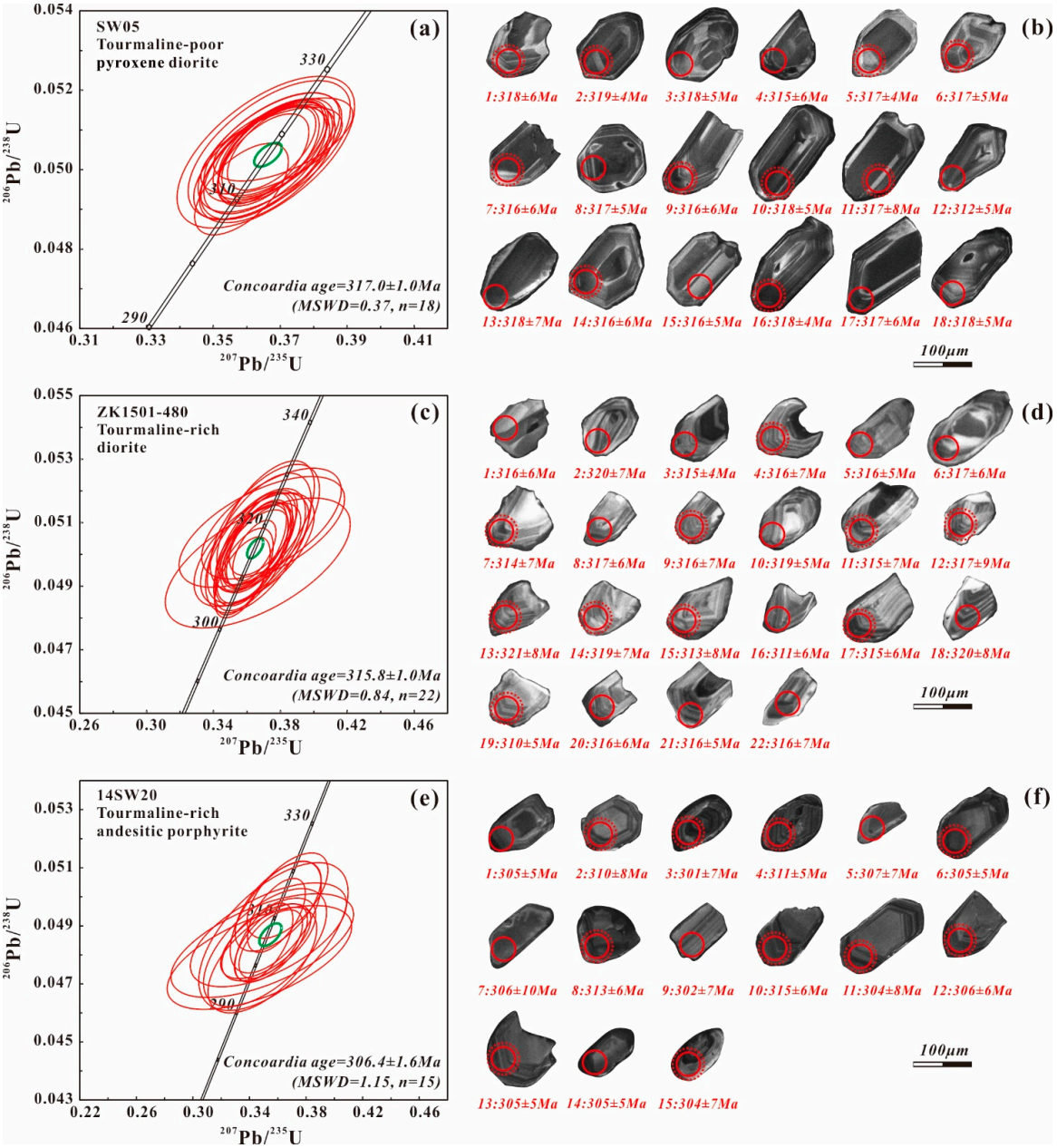

Figure 5. LA–ICP–MS U–Pb concordia age diagrams with CL photos of zircons of tourmaline-poor pyroxene diorite (**a**,**b**), tourmaline-rich diorite (**c**,**d**), and tourmaline-rich andesite (**e**,**f**) in the Shiwu deposit. The solid ellipses and dotted circles in CL photos of zircons represent the analytical location of U-Pb age and the Lu-Hf isotope, respectively. The numbers under CL photos show the plot number (n) with $^{206}Pb/^{238}U$ age data.

4.2. Zircon Hf Isotopes

Hf isotope analyses of zircon grains from the tourmaline-poor pyroxene diorite (sample SW05) yielded $^{176}Lu/^{177}Hf$ ratios of 0.000804–0.001956 and $^{176}Hf/^{177}Hf$ ratios of 0.282755–0.282965. The calculated $_{\varepsilon Hf}(t)$ values range from +6.0 to +13.6, whereas T_{DM2}(Hf) ages vary from 945 to 459 Ma. Zircons from the tourmaline-rich diorite (sample ZK1501-480) have $^{176}Lu/^{177}Hf$ ratios ranging from 0.000635 to 0.001724 and $^{176}Hf/^{177}Hf$ ratios ranging from 0.282961 to 0.283045, with $_{\varepsilon Hf}(t)$ ratios varying from +13.3 to +16.1 and T_{DM2}(Hf) ages varying from 476 to 292 Ma. The tourmaline-rich andesite (sample SW20) shows $^{176}Lu/^{177}Hf$ ratios of 0.000842–0.001689 and $^{176}Hf/^{177}Hf$ ratios of 0.283049–0.283098, $_{\varepsilon Hf}(t)$ ratios of +16.3–+17.9, and T_{DM2}(Hf) ages of 280 to 176 Ma (Figure 6).

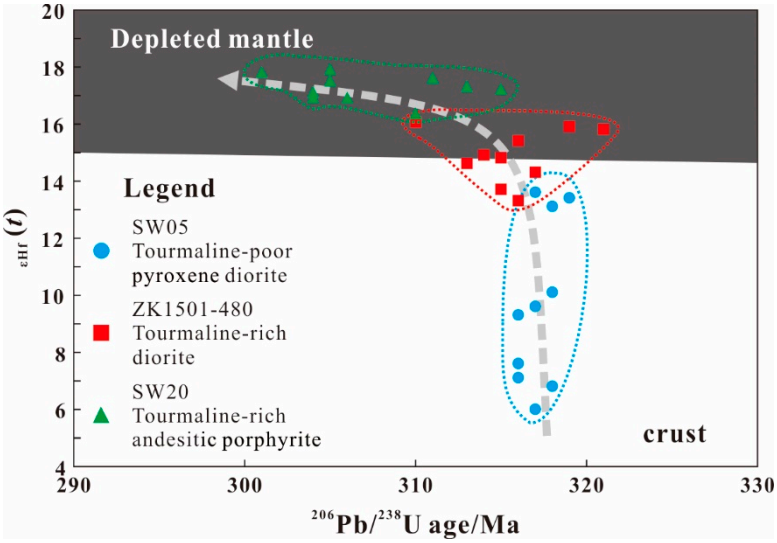

Figure 6. $^{206}Pb/^{238}U$ (Ma)–versus–$_{\varepsilon Hf}(t)$ diagram of zircons of tourmaline-related igneous rocks in Shiwu deposit. Depleted mantle curve modified from [45].

4.3. Composition of Tourmaline in Terms of Major Elements

The representative tourmaline crystals from the tourmaline-rich diorite (sample ZK1501-480) and andesite (sample SW20) are idiomorphic round to elliptical crystals, ca. 160 μm in size, with an elongation ratio of 2 (Figure 7a,c). They have similar composition in terms of major elements, with SiO_2 contents of 35.62 to 37.22 wt%, Al_2O_3 contents of 27.85 to 33.68 wt%, FeO contents of 8.99 to 15.68 wt%, MgO contents of 3.82 to 5.57 wt%, CaO contents of 0.51 to 1.9 wt%, Na_2O contents of 1.56 to 1.93 wt%, and K_2O contents of 0.02 to 0.11 wt%. The tourmalines from the tourmaline-rich diorite and andesite are all alkali-group tourmalines in the tourmaline classification diagram based on X-site occupancy (Figure 8a) [42]. They are all Fe-enriched and plotted within the schorl field in the Fe/(Mg + Fe)(apfu)–versus–X□/(Na + K + X□)(apfu) diagram (Figure 8b). The average end-member mole fractions were calculated using the Excel spreadsheet of Morgan [46] and provided in Table 3. The Mg–Fe plot shows a linear relationship among the data (Figure 8c), which suggests that the schorl–dravite substitution was crucial for these tourmalines ($FeMg_{-1}$) [41]. The Al^{3+} ion substitutes for Fe^{2+}, Mg^{2+}, and Mn^{2+} on the Y-site; charge balance is maintained by changes in the number of vacant X-sites. This substitution relates to the $^{Y}AlX\square(R^{2+}Na)_{-1}$ vector. The Al^{tot}(apfu)–versus–X□(apfu) diagram illustrates a distinctly linear relationship of tourmaline plots (Figure 8d). This variation trend is well interpreted by the $YX\square(R^{2+}Na)_{-1}$ substitution [41,42]. Therefore, the test samples can be classified as alkali (Figure 8a) schorl (Fe-rich tourmaline, Figure 8c,d). Moreover, their parent igneous rocks are granitoids (Figure 9a).

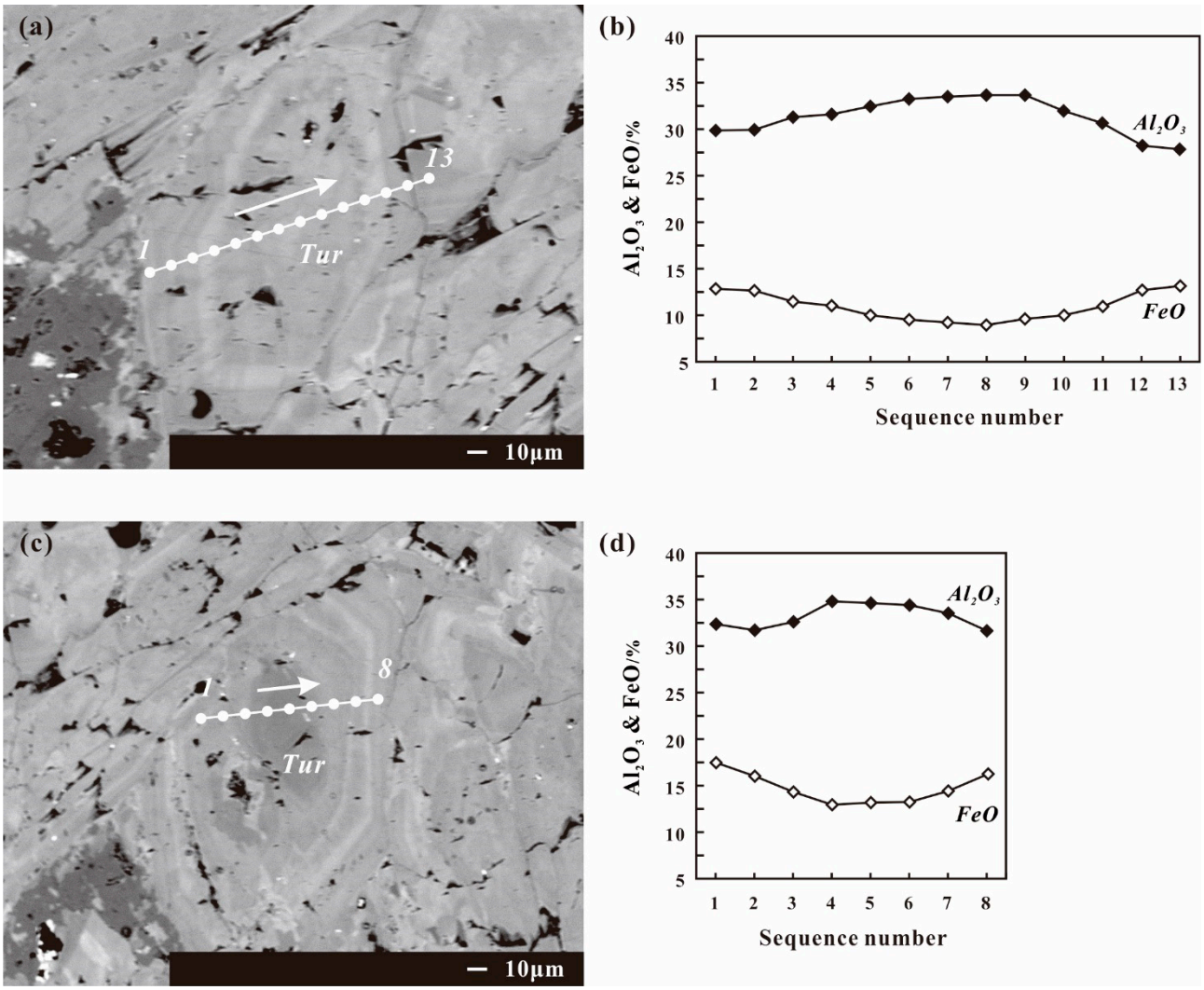

Figure 7. Backscattered electron (BSE) images and measured EPMA cross profiles of the representative tourmaline. Tourmaline crystal with distinct growth zoning (**a**) and its measured profile results of Al_2O_3 and FeO in tourmaline-rich diorite (**b**); Tourmaline crystal with distinct growth zoning and core (**c**) and its measured profile results of Al_2O_3 and FeO in tourmaline-rich andesite (**d**).

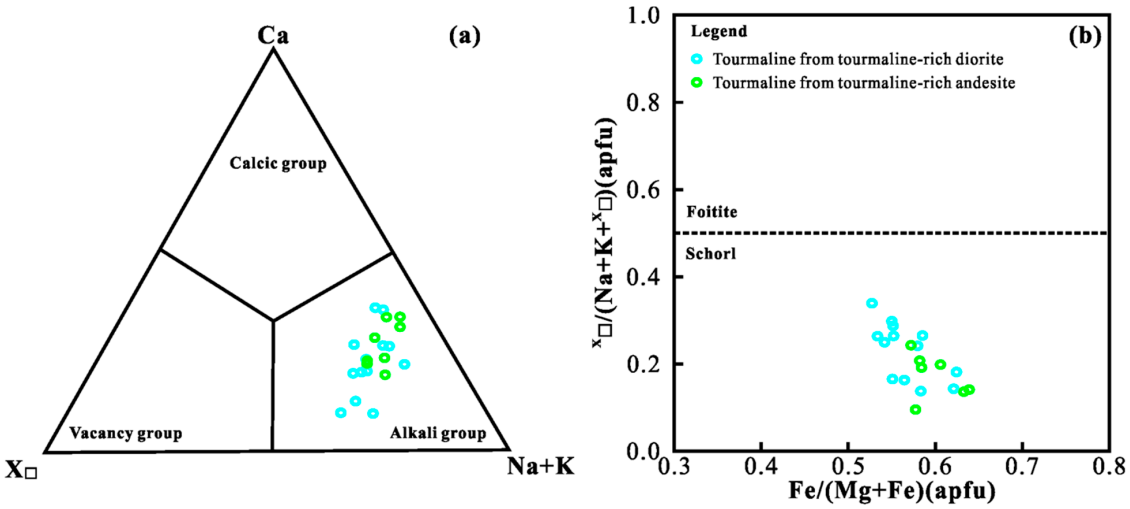

Figure 8. *Cont.*

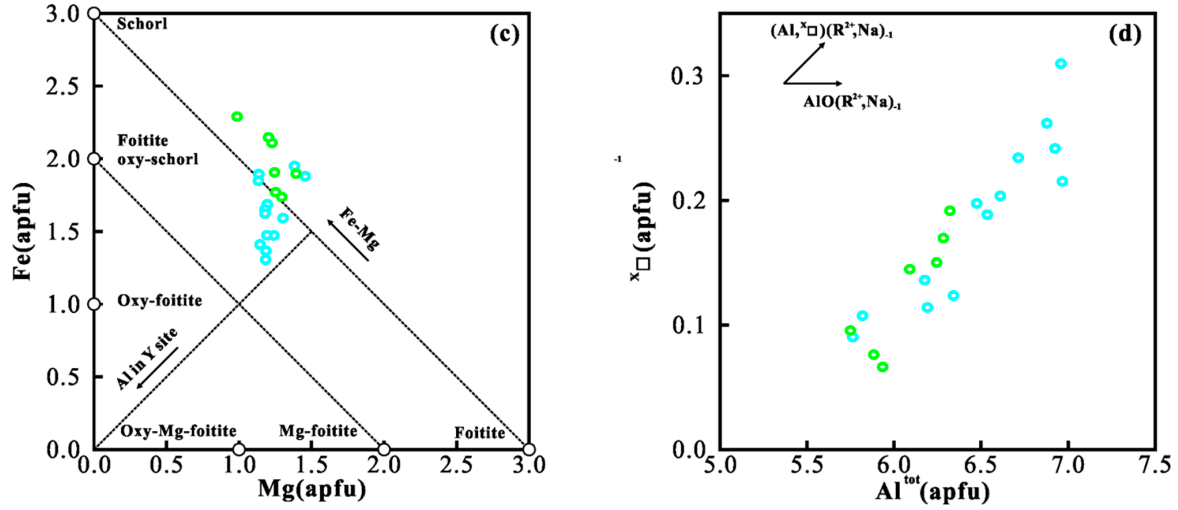

Figure 8. Classification of the principal groups of tourmalines from the tourmaline-rich diorite and andesite based on X-site occupancy ((**a**), modified after [41]). The Fe/(Mg + Fe)(apfu)–versus–X□/(Na + K + X□)(apfu) diagram (**b**), Mg(apfu)–versus–Fe(apfu) diagram (**c**), and Al^{tot}(apfu)–versus–X□(apfu) diagram (**d**) (modified after [42,47]) showing exchange vectors and compositional variations in tourmalines from the tourmaline-rich diorite and andesite in Shiwu deposit. X□ represents the proportions of vacancies at X-site. R^{2+} = Fe + Mg + Mn, and Fe is dominant in R^{2+}. apfu = atom per formula unit.

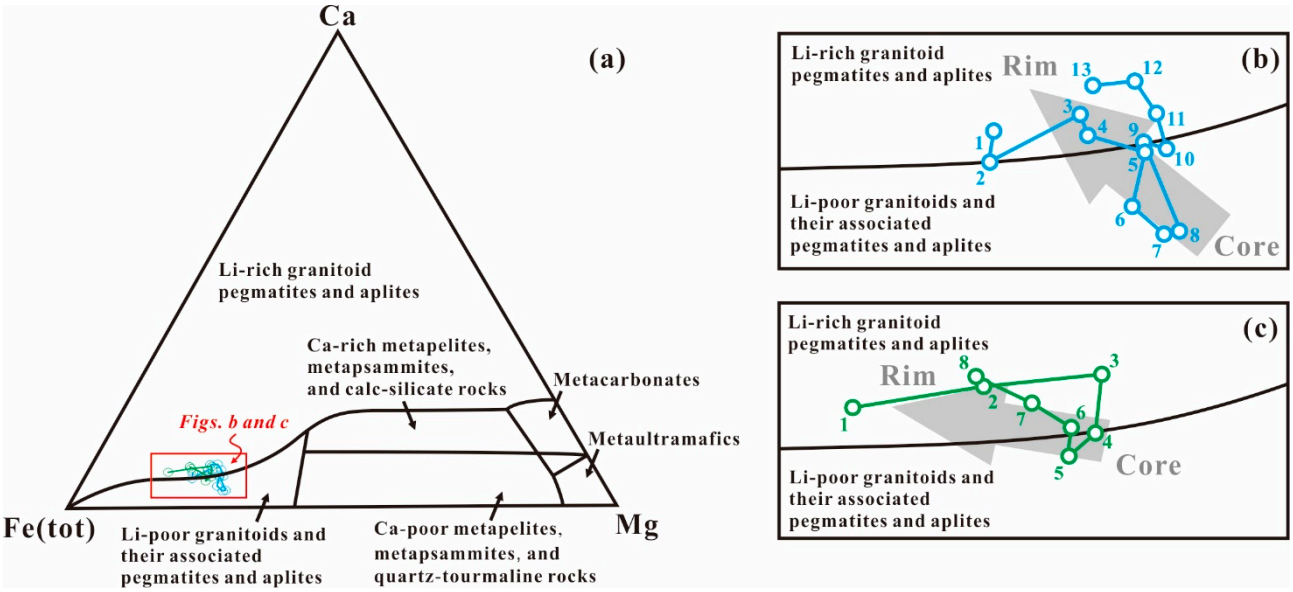

Figure 9. Ca–Fe(tot)–Mg diagram (**a**), modified after [48]) and its enlargements for tourmalines from tourmaline-rich diorite (**b**) and andesite (**c**).

5. Discussion

5.1. Petrogenesis of Tourmaline-Rich Igneous Rocks

5.1.1. Formation Period

In the Shiwu porphyry Cu–Au deposit, voluminous Late Carboniferous gabbroic–granitic (mafic–felsic) intrusions (324–302 Ma) [18,28–30] and minor felsic lavas (e.g., rhyolite, 311 ± 1 Ma) [18] are present. Petrological and geochronological studies of these magmatic rocks have been presented in this paper and elsewhere to reveal the regional tectonic evolution and Cu–Au mineralization associated with these igneous rocks, mostly focusing on the granitoids (see also, [14,28,30,49]). Moreover, two-stage subduction-related

magmatic activity (at ca. 324–311 Ma and ca. 311–302 Ma) has been identified in the Barluk arc [18,26]. The felsic dominant igneous rocks that are ca. 324 Ma to 311 Ma old have variously been interpreted to be related to normally westward subduction of the Junggar Ocean beneath the Kazakhstan Continent, which mainly derives from mixtures of the metasomatized mantle with minor crust contamination [18,28–30]. Conversely, more juvenile mantle materials participated in the creation of the ca. 311 Ma to 302 Ma old mafic dominant igneous rocks, which were probably triggered by subducted oceanic crust slab breakoff and accompanying asthenospheric upwelling and basaltic underplating [18,29]. These theories were also proposed in support of the interpretive genesis of the Suyunhe porphyry Mo deposit (ca. 55 km west of the Shiwu porphyry Cu–Au deposit, Barluk arc) [15,50].

In this study, the obtained tourmaline-rich diorite (sample ZK1501-480) and andesite (sample SW20) had formation ages of 315.8 ± 1.0 Ma and 306.4 ± 1.6 Ma, respectively, indicating that the tourmaline-rich magma emplacement age for the intrusions was ca. 316–306 Ma. Our tourmaline-poor diorite sample (SW05) gave a zircon U–Pb age of 317.0 ± 1.0 Ma, indicating that the precursor magma (ca. 80 vol% of the study area) [18,29,30] came from the normally westward subduction and coeval tectonothermal event. This period is unrelated to the enrichment of volatiles and sulfide. Thus, the production and emplacement of the tourmaline-rich igneous rocks in the Shiwu porphyry Cu–Au deposit might have occurred during the tectonic setting from normal subduction switch to slab breakoff. In other words, a magma source (reservoir) unusually rich in volatiles and chalcophile elements was probably founded or activated by geodynamic variations during the tectonic transition stage. The similar interpretation has been considered in the adjacent Baogutu area, West Junggar [20,51].

5.1.2. Source Characteristics

Limited Hf variations in the isotopic compositions of the tourmaline-rich diorite and andesite ($_{\varepsilon Hf}(t)$ values range from +13.3 to +17.9) are consistent with the tourmaline-poor pyroxene diorite ($_{\varepsilon Hf}(t)$ values range from +6.0 to +13.6) and other intrusions ($_{\varepsilon Hf}(t)$ values range from +4.5 to +15.7) [18,30] in the Shiwu porphyry Cu–Au deposit and suggest that these variations could not have resulted from crustal contamination during magma ascent or emplacement [20,51]. Therefore, geochemical signatures can be used to indicate the nature of the source of Shiwu tourmaline-rich igneous rocks.

The extremely young zircon T_{DM2}(Hf) ages (476 to 176 Ma) of Shiwu tourmaline-rich diorite (sample ZK1501-480) and andesite (sample SW20) suggest the presence of juvenile mafic lower crust or other juvenile mantle materials [18,30]. However, the relatively older T_{DM2}(Hf) age (945 Ma) indicates that the tourmaline-poor pyroxene diorite (sample SW05) in Shiwu was derived from a mixture of juvenile mantle materials and >0.9 Ga crustal components [18,52,53].

As illustrated in Figure 6, the tourmaline-poor pyroxene diorite (sample SW05) and the tourmaline-rich diorite (sample ZK1501-480) and andesite (sample SW20) exhibit a well-defined linear covariation between $^{206}Pb/^{238}U$ (Ma) and $_{\varepsilon Hf}(t)$. This variation may reflect a source heterogeneity, and it could not have resulted from the fractional crystallization of a common parental magma.

5.1.3. Involvement of the Mantle Component

All geochemical studies of Late Carboniferous igneous rocks from the Barluk continental arc show distinct subduction-related signatures [14,18,24–33]. Wu et al. [18] further suggested the igneous rocks in the Shiwu area before 310 Ma with crust-mantle mixing characteristics that originated from a typical continental arc during its subduction process. Some ca. 302 Ma mafic rocks there with more positive Nd and Hf isotopic characteristics ($_{\varepsilon Nd}(t)$ = ca. +7.5 and $_{\varepsilon Hf}(t)$ = +12.8–+15.5) were related to the upwelling of asthenosphere mantle in a post-subduction extensional tectonic setting. The tourmaline-poor pyroxene diorite (sample SW05, 317.0 ± 1.0 Ma) represents the precursor magmatic activity in the

Shiwu porphyry Cu–Au deposit. Its $_{\varepsilon Hf}(t)$ values are plotted below the depleted mantle line on the $^{206}Pb/^{238}U$ (Ma)-versus-$_{\varepsilon Hf}(t)$ diagram (Figure 6), which suggests minor contamination by an old crust. In contrast, the younger tourmaline-rich diorite (sample ZK1501-480, 315.8 ± 1.0 Ma) and andesite (sample SW20, 306.4 ± 1.6 Ma) are mainly derived from juvenile mantle materials and rarely have old crustal components joined in the source mixture. That is, the tourmaline-poor pyroxene diorite has relatively lower $_{\varepsilon Hf}(t)$ values than tourmaline-rich diorite and andesite. The $_{\varepsilon Hf}(t)$ values from +13.3 to +17.9 in tourmaline-rich diorite and andesite are consistent with previously reported 302.2 Ma asthenospheric mantle–derived gabbro ($_{\varepsilon Hf}(t)$ from +12.8 to +15.5) [18]. Meanwhile, the tourmaline-poor pyroxene diorite has $_{\varepsilon Hf}(t)$ values that range from +6.0 to +13.6 and are similar to that igneous rocks ($_{\varepsilon Hf}(t)$ from +3.8 to +12.6) formed in normal subduction before 310 Ma [18].

There are two different interpretations for the genesis of tourmaline-rich magma. We suggest that the Hf isotopes of tourmaline-poor pyroxene diorite, tourmaline-rich diorite, and tourmaline-rich andesite in this study recorded the tectonic transform from normal subduction to slab breakoff in the Shiwu area. The tourmaline-rich magma probably formed in the slab breakoff setting due to a slab window. When the slab window opened, the asthenosphere could have upwelled and supplied high temperature and pressure to upper components. This process could have caused the previously subducted oceanic crust, mantle, and overlying juvenile mafic lower crust to extensively melt and mix and produce magmas rich in Shiwu volatiles (tourmaline) and chalcophile elements. The corresponding metamorphism and widespread extension of the crust would have also occurred in the same dynamic and thermodynamic conditions [20,54]. Moreover, the formation of high $_{\varepsilon Hf}(t)$ value and tourmaline-rich magma may be due to a slab subsidence. As the subducted oceanic plate has sunk, the juvenile mantle-derived materials have grown correspondingly in magma source.

Thus, there was increasing involvement of mantle components (juvenile materials) during the formation process of the Shiwu tourmaline-poor pyroxene diorite and tourmaline-rich diorite and andesite. This assumption is also supported by EPMA analyses: the increasing content of FeO with the decreasing content of Al_2O_3 from the inside (core) to the outside (growth zoning) in tourmaline phenocrysts from both tourmaline-rich diorite and andesite (Figure 7b,d).

5.2. Formation Mechanism of the Shiwu Deposit

5.2.1. Tourmaline-Sulfide Mineralization in the Diorite and Andesite

In the magmatic-hydrothermal evolution process, devolatilization and phase separation of hydrous boron-rich fluids unmixed from granitic melts have been interpreted to be the genesis of primary tourmaline in miarolitic cavity in granite [42]. Significant disseminated tourmaline and pyrite assemblages in miarolitic cavities or irregular–shape intergrowth with augen quartz phenocrysts suggests that they were original minerals that crystallized with other silicate minerals in the diorite and andesite. This conclusion is also supported by miarolitic cavity studies and EPMA analyses: (1) previous studies have suggested that disseminated sulfide assemblages in miarolitic cavities in porphyry deposits can record the initial compositions of magmatic–hydrothermal ore-forming fluids [3,55–57]; (2) the interstitial sulfides can represent the original mineral and reflect early stage magmatic–hydrothermal mineralization in porphyry deposits [20,58]; (3) there is abundant field evidence that the miarolitic cavity of tourmaline has a complete border, disproving the hypothesis that veins play a role as conduits to feed or recharge the miarolitic cavity (Figure 3b); (4) the tourmalines are present as idiomorphic round to elliptical grains (160 μm) with a clear core and growth zoning (Figure 7a,c), which suggests that the diorite and the andesite have not been affected by feldspathization and biotitization; and (5) the poor correlation between test locations and K_2O and Na_2O contents also suggests the low-temperature alteration unrelated to mineralization. The boron-rich fluids related to these tourmalines were probably derived from felsic melts without conspicuous contamination.

These pieces of evidence suggest that the boron-rich fluids in the Shiwu porphyry Cu–Au deposit has been trapped beneath the roof of crystallizing granitic sills, which is similar to western Tasmanian granites reported by Hong et al. [42]. Thus, we further propose that there can be a high ore-prospecting potential in the deep of the Shiwu or the Barluk area.

5.2.2. Sulfide-Rich Magmatic–Hydrothermal Evolution

The intergrowths of sulfide with other hydrothermal minerals in the miarolitic cavities suggests that precipitation of the sulfide minerals was coeval with hydrothermal mineralization [3,59]. Therefore, the miarolitic cavities were formed and mineralized during the magmatic–hydrothermal transition and the initial ore fluids were rich in sulfides. Moreover, tourmaline is stable over a wide range of conditions: low-temperature hydrothermal alterations, high-grade and high-pressure metamorphic environments, or magmatic conditions [10].

Previous studies on mineralization, fluid inclusions, and S isotopes in the Shiwu porphyry Cu–Au deposit have also suggested that the ore-forming fluid is closely related to magmatism and further indicated that the ore-forming fluid is mainly derived from the upper mantle or the juvenile mafic lower crust [14]. The cores of the tourmaline plot within a Li-poor granitoid field have relatively low FeO contents and indicate an ore-poor character (Figure 9a,b). This suggests that a metal-poor magma dominated the early stage of magmatism. Rims analyses of the same tourmaline located in a Li-rich granitoid field (Figure 9c) indicate an increase in the quantity of the metal. Increased FeO and decreased Al_2O_3 in tourmaline growth zoning (Figure 7b,d) and consistent augmentation of $_{\varepsilon Hf}(t)$ in zircons from the tourmaline-poor pyroxene diorite and the tourmaline-rich diorite and andesite (Figure 6) further reveal an injection of mantle-derived and ore-rich magma. This conclusion is also supported by the evolutionary trends of tourmalines in the tourmaline-rich diorite and andesite (Figure 8c,d).

5.2.3. Ore-Forming Process

The injection of mantle-derived and ore-rich magma during the tectonic transition stage was critical for the formation of the Shiwu porphyry Cu–Au deposit. Magma produced during the early normal subduction could have been metal poor. As geodynamical switching (e.g., the tectonic setting transformed from normal subduction into slab breakoff, a slab window opening or subducted oceanic slab subsidence), an unusually ore-rich reservoir could have been founded or activated to produce magma rich in volatile and chalcophile elements. However, with an increase in reduced components from the asthenospheric mantle in the magmatic mixture, the metal could have been depleted rapidly at the source or during transportation [20,58,60–62]. Moreover, gold transport is largely mechanical, in the form of colloidal particles or flocculate masses [63–65], and the early crystallized sulfides could also travel as sulfide globules in the ore-fluid [66]. These processes crucially contributed to subsequent magmatic–hydrothermal mineralization. Thus, the mineralization of the Shiwu porphyry Cu–Au deposit is concentrated in tourmaline-rich igneous rocks (such as dikes, veins, and veinlets) but decentralized in other wallrock.

5.3. Implication for the Tectonic Setting of the Barluk Arc

On the basis of positive $_{\varepsilon Nd}(t)$ and $_{\varepsilon Hf}(t)$ values with young zircons, most perspectives support that Barluk igneous rocks were formed in the island arc background, tectonically located in the Junggar Ocean [26,28,32,67]. However, tourmaline is an important prospecting guide particularly associated with porphyry Sn/Sn–W deposits that formed in the post-collisional setting [68]. Tourmalines in porphyry Cu mineralized systems are normally in breccia pipes and the sodic alteration zone [12,69], and most of these porphyry Cu deposits are formed in the continental marginal arc setting [2,6,7,12,70]. Therefore, the presence of numerous tourmalines in the Shiwu porphyry Cu–Au deposit implies a continental arc setting.

Previous tectonic, petrogenesis, geochemical, and geochronological characteristics also indicate that the igneous rocks in the Barluk region formed in a continental arc setting and were located along the margin of the Kazakhstan Continent [18]. The characteristics are as follows:

(1) The Barluk arc is spatially associated with the old continent and is located along the southeastern margin of the Kazakhstan Continent [16,18,71].
(2) The widely distributed calc-alkaline series igneous rocks in the Barluk arc are normally characterized by the enrichment of Zr and Hf and relatively low $_{\varepsilon Nd}(t)$ and $_{\varepsilon Hf}(t)$ values (low to +4.6 and +3.8, respectively) [18,28,30], characteristics that have a strong affinity to the Andean-type continental arc.
(3) Abundant ancient zircons, both from the Shiwu and northeastern parts (0.76–2.51 Ga) [18,72], in the Barluk arc also document that the Barluk arc contains Precambrian basement crust or materials.

5.4. Respect to the Potential Porphyry-Type Mineralization in the Barluk Arc

The Baogutu porphyry Cu–Mo–Au deposit [58] and Hongyuan porphyry Mo-Cu deposit [73] in the adjacent Baogutu arc and the Suyunhe porphyry Mo-Cu deposit within in the Barluk arc [15] were three special and typical "reduced" porphyry-type deposits in the West Junggar. They are characterized by the lack of primary hematite and sulfate minerals (i.e., anhydrite), but contain abundant hypogene pyrrhotite and substantial CH_4-rich ore-forming fluid, in accordance with the characteristics of reduced porphyry Cu deposit described by Rowins [74]. The reduced ore-forming system normally restricted the enrichment and migration of chalcophile elements [75], lead to the relatively reserved and low grade of porphyry Cu-related resource in the West Junggar domain. In general, the variation of valence of sulfur, which has been controlled by the oxidation and reduction in ore-forming fluid, plays an important role during the enrichment, migration, and deposition process of the chalcophile elements. The volatile component is a crucial factor in the formation of porphyry-type deposits [42]. The high concentrations of volatile promote the metal dissolution and migration in ore-forming magmatic-hydrothermal fluids [76,77]. The presence of numerous tourmalines in the Shiwu porphyry Cu–Au deposit reflects a high concentration of volatile (e.g., B, F, and Li) in its magmatic-hydrothermal system [42]. Moreover, most enrichment, migration, and deposition of Mo and Au are probably controlled by the combined action of the valence fluctuations of S and Cl [75,78]. Part of the early crystallized sulfides could travel and deposit as sulfide globules (e.g., activated metal complexing compound or granular Au) which are also crucially contributed to the final porphyry mineralization [20,75]. Therefore, we propose that there is a molybdenum (gold) polymetallic ore potential of porphyry series in the depth of Barluk arc, meanwhile, the primary tourmaline can be used as a prospecting guide.

6. Conclusions

(1) The tourmaline-poor pyroxene diorite, the tourmaline-rich diorite, and the tourmaline-rich andesite in the Shiwu porphyry Cu–Au deposit indicate zircon ages of 317.0 ± 1.0 Ma (MSWD = 0.37, n = 18), 315.8 ± 1.0 Ma (MSWD = 0.84, n = 22), and 306.4 ± 1.6 Ma (MSWD = 1.15, n = 15), respectively. They were probably constrained by the tectonic converting of Late Carboniferous subduction in the Barluk continental arc.
(2) The tourmaline-poor pyroxene diorite and other precursor igneous rocks in the Shiwu porphyry Cu–Au deposit is produced by a mixture of juvenile mantle materials and old crustal components in varying proportions. The tourmaline-rich diorite and the tourmaline-rich andesite are mainly sourced from juvenile mantle materials. More and more mantle-derived components join in the formation process of the Shiwu tourmaline-poor pyroxene diorite, tourmaline-rich diorite, and andesite.
(3) The higher mantle influence was associated with generation of boron-rich fluids that might have also supplied the large amount of copper and gold required to generate significant the Cu–Au mineralization in the Shiwu porphyry Cu–Au deposit.

Author Contributions: C.W. (Chu Wu), C.W. (Chengxi Wang). and T.H., conceived of the presented idea. C.W. (Chu Wu) and T.H. conducted the experiment. All authors, C.W. (Chu Wu), C.W. (Chengxi Wang)., T.H., X.X., X.Z., W.L., K.S., H.Z., L.D. and B.W., discussed the results and contributed to the final manuscript. All authors have read and agreed to the published version of the manuscript.

Funding: This research was jointly supported by the Project of Development and Research Center of China Geology Survey (DD20221785 and DD20230600), the National Natural Science Foundation of China (41802093, 42272075 and 42250202), the Basic and Applied Basic Research Foundation of Guangdong Province (2022A1515010003), and the Project of Xinjiang Bureau of Geology and Mineral Resources (2011BAB06B03-3).

Data Availability Statement: The original contributions presented in the study are all included in the article.

Acknowledgments: We acknowledge Guoliang Zhang, Jun You, Hao Li, and Hang Li for their support during the field work and for their professional input. Mingjian Cao, Bo Xu, and Xijie Chen are thanked for their valuable discussions. This paper was especially and significantly improved by Pete Hollings. Moreover, the first author wants to thank his wife Yan Liu, child Pei-zhou Wu, and forthcoming baby Miao-xi Wu for their encouragement.

Conflicts of Interest: The authors declare no conflict of interest.

References

1. Seedorff, E.; Dilles, J.H.; John, M.; Proffett, J.; Einaudi, M.T.; Zurcher, L.; Stavast, W.J.A.; Johnson, D.A.; Barton, M.D. Porphyry deposits: Charcteristics and origin of hypogene features. In *Economic Geology One Hundredth Anniversary Volume 1905–2005*; Hedenquist, J.W., Thompson, J.F.H., Goldfarb, R.J., Richards, J.P., Eds.; Society of Economic Geologists: Littleton, CO, USA, 2005; pp. 251–298.
2. Sillitoe, R.H. Porphyry Copper Systems. *Econ. Geol.* **2010**, *105*, 3–41. [CrossRef]
3. Xu, X.W.; Li, H.; Peters, S.G.; Qin, K.Z.; Mao, Q.; Wu, Q.; Hong, T.; Wu, C.; Liang, G.L.; Zhang, Z.F.; et al. Cu-rich porphyry magmas produced by fractional crystallization of oxidized fertile basaltic magmas (Sangnan, East Junggar, PR China). *Ore Geol. Rev.* **2017**, *91*, 296–315. [CrossRef]
4. Hong, T.; Xu, X.W.; Gao, J.; Peters, S.G.; Zhang, D.; Jielili, R.; Xiang, P.; Li, H.; Wu, C.; You, J.; et al. Ore-forming adakitic porphyry produced by fractional crystallization of oxidized basaltic magmas in a subcrustal chamber (Jiamate, East Junggar, NW China). *Lithos* **2018**, *296–299*, 96–112. [CrossRef]
5. Slack, J.F. Tourmaline associations with hydrothermal ore deposits. *Rev. Mineral.* **1996**, *33*, 559–643. [CrossRef]
6. Lynch, G.; Ortega, J. Hydrothermal alteration and tourmaline-albite equilibria at the Coxheath porphyry Cu-Mo-Au deposit, Nova Scotia. *Can. Mineral.* **1997**, *35*, 79–94.
7. Baksheev, I.A.; Yu Prokof'Ev, V.; Zaraisky, G.P.; Chitalin, A.F.; Yapaskurt, V.O.; Nikolaev, Y.N.; Tikhomirov, P.L.; Nagornaya, E.V.; Rogacheva, L.I.; Gorelikova, N.V.; et al. Tourmaline as a prospecting guide for the porphyry-style deposits. *Eur. J. Mineral.* **2012**, *24*, 957–979. [CrossRef]
8. Harlaux, M.; Kouzmanov, K.; Gialli, S.; Laurent, O.; Rielli, A.; Dini, A.; Chauvet, A.; Menzies, A.; Kalinaj, M.; Fontboté, L. Tourmaline as a Tracer of Late-Magmatic to Hydrothermal Fluid Evolution: The World-Class San Rafael Tin (-Copper) Deposit, Peru. *Econ. Geol.* **2020**, *115*, 1665–1697. [CrossRef]
9. Aysal, N.; Ongen, S.; Hanilci, N.; Kasapci, C.; Lacin, D.; Boroglu, M.S.; Yesiltas, M.; Yilmaz, I.; Azaz, D. Late magmatic–hydrothermal tourmaline occurrences within leucogranites in NW Anatolia (Turkey): Mineral chemistry and genetic implications. *Geochem. Interdiscip. J. Chem. Probl. Geosci. Geoecol.* **2021**, *81*, 125676-1–125676-16. [CrossRef]
10. Baksheev, I.A.; Chitalin, A.F.; Yapaskurt, V.O.; Vigasina, M.F.; Bryzgalov, I.A.; Ustinov, V.I. Tourmaline in the Vetka Porphyry Copper–Molybdenum Deposit of the Chukchi Peninsula of Russia. *Mosc. Univ. Geol. Bull.* **2010**, *65*, 27–38. [CrossRef]
11. Landtwing, M.R.; Dillenbeck, E.D.; Leake, M.H.; Heinrich, C.A. Evolution of the Breccia-Hosted Porphyry Cu-Mo-Au Deposit at Agua Rica, Argentina: Progressive Unroofing of a Magmatic Hydrothermal System. *Econ. Geol.* **2002**, *97*, 1273–1292. [CrossRef]
12. Yavuz, F.; Iskenderoglu, A.; Jiang, S.Y. Tourmaline compositions from the Salikvan porphyry Cu-Mo deposit and vicinity, northeastern Turkey. *Can. Mineral.* **1999**, *37*, 1007–1023.
13. Bozkaya, G.; Hanilçi, N.; Baksheev, I.A.; Prokofiev, V.Y.; Banks, D.A. Tourmaline Composition of the Kışladağ Au Deposit, Uşak, Turkey. *Acta Geol. Sin-Engl.* **2014**, *88*, 520–521. [CrossRef]
14. Li, C.H.; Shen, P.; Pan, H.D.; Huang, W.; Cao, C. Geology, ore-forming fluids and potential of Shiwu porphyry Cu-Au spot in West Junggar, Xinjiang. *Miner. Depos.* **2017**, *36*, 816–836. (In Chinese with English Abstract)
15. Cao, C.; Shen, P.; Pan, H.D.; Zheng, L.M.; Li, C.H.; Feng, H.X. The formation mechanism of reduced porphyry Mo deposits in the West Junggar region, Xinjiang: The Suyunhe example. *Ore Geol. Rev.* **2020**, *117*, 103286. [CrossRef]
16. Windley, B.F.; Alexeiev, D.; Xiao, W.J.; Kroner, A.; Badarch, G. Tectonic models for accretion of the Central Asian Orogenic Belt. *J. Geol. Soc. Lond.* **2007**, *164*, 31–47. [CrossRef]

17. Xu, X.W.; Jiang, N.; Li, X.H.; Wu, C.; Qu, X.; Zhou, G.; Dong, L.H. Spatial-temporal framework for the closure of the Junggar Ocean in Central Asia: New SIMS zircon U-Pb ages of the ophiolitic mélange and collisional igneous rocks in the Zhifang area, East Junggar. *J. Asian Earth Sci.* **2015**, *111*, 470–491. [CrossRef]
18. Wu, C.; Hong, T.; Xu, X.W.; Cao, M.J.; Li, H.; Zhang, G.L.; You, J.; Ke, Q.; Dong, L.H. Tectonic evolution of the Paleozoic Barluk continental arc, West Junggar, NW China. *J. Asian Earth Sci.* **2018**, *160*, 48–66. [CrossRef]
19. Wu, C.; Hong, T.; Xu, X.W.; Li, H.; Ke, Q.; Li, H.; Dong, L.H. Constraints on the nature of the basement of the Junggar terrane indicated by the Laba Ordovician continental arc. *Int. Geol. Rev.* **2020**, *62*, 29–52. [CrossRef]
20. Wu, C.; Hong, T.; Xu, X.W.; Cao, M.J.; Li, H.; Ke, Q.; Li, H.; Dong, L.H. Constraints on the formation of the Baogutu reduced porphyry copper deposit (West Junggar, NW China): Assessing the role of mafic magmas in mineralization. *Lithos* **2019**, *336–337*, 112–124. [CrossRef]
21. Xu, X.W.; Jiang, N.; Li, X.H.; Qu, X.; Yang, Y.H.; Mao, Q.; Wu, Q.; Zhang, Y.; Dong, L.H. Tectonic evolution of the East Junggar terrane: Evidence from the Taheir tectonic window, Xinjiang, China. *Gondwana Res.* **2013**, *24*, 578–600. [CrossRef]
22. Zhu, Y.F.; Chen, B.; Xu, X.; Qiu, T.; An, F. A new geological map of the western Junggar, north Xinjiang (NW China): Implications for Paleoenvironmental reconstruction. *Episodes* **2013**, *36*, 205–220. [CrossRef] [PubMed]
23. Sengör, A.M.C.; Natal'in, B.A. Paleotectonics of Asia: Fragments of a synthesis. In *The Tectonic Evolution of Asia*; Rubey Colloquium; Yin, A., Harrison, M., Eds.; Cambridge University Press: Cambridge, UK, 1996; pp. 486–640.
24. Yang, G.X.; Li, Y.J.; Yang, B.K.; Wang, H.B.; Zhang, H.W.; Tong, L.L. Geochemstry of basalt from the Barleik ophiolitic mélange in West Junggar and its tectonic implications. *Acta Geol. Sin.* **2012**, *86*, 188–197. (In Chinese with English Abstract)
25. Zhao, W.P.; Jia, Z.K.; Wen, Z.G.; Li, Y.J. The discovery of blueschists from the Baerluke ophiolitic mélange belt in western Junggar, Xinjiang. *Northwestern Geol.* **2012**, *45*, 136–138. (In Chinese with English Abstract)
26. Xu, Z.; Han, B.F.; Ren, R.; Zhou, Y.Z.; Su, L. Palaeozoic multiphase magmatism at Barleik Mountain, southern West Junggar, Northwest China: Implications for tectonic evolution of the West Junggar. *Int. Geol. Rev.* **2013**, *55*, 633–656. [CrossRef]
27. Liu, B.; Han, B.F.; Xu, Z.; Ren, R.; Zhang, J.R.; Zhou, J.; Su, L.; Li, Q.L. The Cambrian initiation of intra-oceanic subduction in the southern Paleo-Asian Ocean: Further evidence from the Barleik subduction-related metamorphic complex in the West Junggar region, NW China. *J. Asian Earth Sci.* **2016**, *123*, 1–21. [CrossRef]
28. Li, C.H.; Shen, P.; Pan, H.D.; Huang, W.; Cao, C. Carboniferous porphyry Cu (-Au) mineralization of the West Junggar region, NW China: The Shiwu example. *Int. Geol. Rev.* **2017**, *59*, 1175–1194. [CrossRef]
29. Liu, B.; Han, B.F.; Ren, R.; Chen, J.F.; Wang, Z.Z.; Zheng, B. Petrogenesis and tectonic implications of the Early Carboniferous to the Late Permian Barleik plutons in theWest Junggar (NW China). *Lithos* **2017**, *272–273*, 232–248. [CrossRef]
30. Hu, Y.; Wang, J.L.; Wang, J.Q.; Ling, W.W. Origin of the Shiwu pluton in Barluk region, Xinjiang: Zircon U-Pb chronological, geochemical and Sr-Nd-Pb-Hf isotopic constraints. *Acta Petrol. Sin.* **2018**, *34*, 601–617. (In Chinese with English Abstract)
31. Liu, B.; Han, B.F.; Xu, Z.; Ren, R.; Chen, J.F. The Ediacaran to Early Palaeozoic evolution of the Junggar–Balkhash Ocean: A synthesis of the ophiolitic mélanges in the southern West Junggar terrane, NW China. *Geol. J.* **2019**, *55*, 1689–1707. [CrossRef]
32. Shen, P.; Xiao, W.J.; Pan, H.D.; Dong, L.H.; Li, C.F. Petrogenesis and tectonic settings of the Late Carboniferous Jiamantieliek and Baogutu ore-bearing porphyry intrusions in the southern West Junggar, NW China. *J. Asian Earth Sci.* **2013**, *75*, 158–173. [CrossRef]
33. Shen, P.; Pan, H.D.; Cao, C.; Zhong, S.H.; Li, C.H. The formation of the Suyunhe large porphyry Mo deposit in the West Junggar terrain, NW China: Zircon U-Pb age, geochemistry and Sr-Nd-Hf isotopic results. *Ore Geol. Rev.* **2017**, *81*, 808–828. [CrossRef]
34. FRGSBX (First Regional Geological Survey Brigade of Xinjiang). *The Investigative Project Design of Shiwu Cu-Au Deposit, Tuoli, Xinjiang*; Project number XGMB2013002; National Geological Archives of China: Beijing, China, 2014; pp. 1–120.
35. Xie, L.W.; Zhang, Y.B.; Zhang, H.H.; Sun, J.F.; Wu, F.Y. In situ simultaneous determination of trace elements, U-Pb and Lu-Hf isotopes in zircon and baddeleyite. *Chin. Sci. Bull.* **2008**, *53*, 1565–1573. [CrossRef]
36. Anderson, T. Correction of common lead in U-Pb analyses that do not report ^{204}Pb. *Chem. Geol.* **2002**, *192*, 59–79. [CrossRef]
37. Ludwig, K.R. *SQUID 1.02: A User's Manual*; Special Publication 2; Berkeley Geochronology Center: Berkeley, CA, USA, 2001; pp. 1–19.
38. Wu, F.Y.; Yang, Y.H.; Xie, L.W.; Yang, J.H.; Xu, P. Hf isotopic compositions of the standard zircons and baddeleyites used in U-Pb geochronology. *Chem. Geol.* **2006**, *234*, 105–126. [CrossRef]
39. Goolaerts, A.; Mattielli, N.; de Jong, J.; Weis, D.; Scoates, J.S. Hf and Lu isotopic reference values for the zircon standard 91500 by MC-ICP-MS. *Chem. Geol.* **2004**, *206*, 1–9. [CrossRef]
40. Woodhead, J.; Hergt, J.; Shelley, M.; Eggins, S.; Kemp, R. Zircon Hf-isotope analysis with an excimer laser, depth profiling, ablation of complex geometries, and concomitant age estimation. *Chem. Geol.* **2004**, *209*, 121–135. [CrossRef]
41. Henry, D.J.; Novak, M.; Hawthorne, F.C.; Ertl, A.; Dutrow, B.L.; Uher, P.; Pezzotta, F. Nomenclature of the tourmaline-supergroup minerals. *Am. Mineral.* **2011**, *96*, 895–913. [CrossRef]
42. Hong, W.; Cook, D.R.; Zhang, L.J.; Fox, N.; Thompson, J. Tourmaline-rich features in the Heemskirk and Pieman Heads granites from western Tasmania, Australia: Characteristics, origins, and implications for tin mineralization. *Am. Mineral.* **2017**, *102*, 876–899. [CrossRef]
43. Hoskin, P.W.O.; Black, L.P. Metamorphic zircon formation by solid-state recrystallization of protolith igneous zircon. *J. Metamorph. Geol.* **2000**, *18*, 423–439. [CrossRef]
44. Corfu, F.; Hanchar, J.M.; Hoskin, P.W.O.; Kinny, P. Atlas of zircon textures. *Rev. Mineral. Geochem.* **2003**, *53*, 469–500. [CrossRef]

45. Bodet, F.; Schärer, U. Evolution of the SE-Asian continent from U-Pb and Hf isotopes in single grains of zircon and baddeleyite from large rivers. *Geochim. Cosmochim. Acta* **2000**, *64*, 2067–2091. [CrossRef]
46. Morgan, G.B. A spreadsheet for calculating normative mole fractions of end-member species for Na-Ca-Li-Fe^{2+}-Mg-Al tourmalines from electron microprobe data. *Am. Mineral.* **2016**, *101*, 111–119. [CrossRef]
47. Hong, T.; Zhai, M.G.; Xu, X.W.; Li, H.; Wu, C.; Ma, Y.C.; Niu, L.; Ke, Q.; Wang, C. Tourmaline and quartz in the igneous and metamorphic rocks of the Tashisayi granitic batholith, Altyn Tagh, northwestern China: Geochemical variability constraints on metallogenesis. *Lithos* **2021**, *400–401*, 106358. [CrossRef]
48. Henry, D.J.; Guidotti, C.V. Tourmaline as a petrogenetic indicator mineral: An example from the staurolite-grade metapelites of NW Maine. *Am. Mineral.* **1985**, *70*, 1–15.
49. Li, C.H.; Shen, P.; Huang, W. Geology and fluid inclusion of the Shiwu porphyry Cu-Au deposit in the West Junggar, Xinjiang. *Acta Mineral. Sin.* **2015**, *35*, 481. (In Chinese)
50. Zhong, S.H.; Seltmann, R.; Shen, P. Two different types of granitoids in the Suyunhe large porphyry Mo deposit, NW China and their genetic relationships with molybdenum mineralization. *Ore Geol. Rev.* **2017**, *88*, 116–139. [CrossRef]
51. Cao, M.J.; Qin, K.Z.; Li, G.M.; Evans, N.J.; Hollings, P.; Jin, L.Y. Genesis of ilmenite series I-type granitoids at the Baogutu reduced porphyry Cu deposit, western Junggar, NW-China. *Lithos* **2016**, *246–247*, 13–30. [CrossRef]
52. Clynne, M.A. A complex magma mixing origin for rocks erupted in 1915, Lassen Peak, California. *J. Petrol.* **1999**, *40*, 105–132. [CrossRef]
53. Gao, S.; Rudnick, R.L.; Yuan, H.L.; Liu, X.M.; Liu, Y.S.; Xu, W.L.; Ling, W.L.; Ayers, J.; Wang, X.C.; Wang, Q.H. Recycling lower continental crust in the North China Craton. *Nature* **2004**, *432*, 892–897. [CrossRef]
54. Martin, H.; Smithies, R.H.; Rapp, R.; Moyen, J.F.; Champion, D. An overview of adakite, tonalite-trondhjemite-granodiorite (TTG), and sanukitoid: Relationships and some implications for crustal evolution. *Lithos* **2005**, *79*, 1–24. [CrossRef]
55. Heithersay, P.S.; Walshe, J.L. Endeavour 26 North; a porphyry copper-gold deposit in the Late Ordovician, shoshonitic Goonumbla volcanic complex, New South Wales, Australia. *Econ. Geol.* **1995**, *90*, 1506–1532. [CrossRef]
56. Candela, P.A. A review of shallow, ore-related granites: Textures, volatiles, and ore metals. *J. Petrol.* **1997**, *38*, 1619–1633. [CrossRef]
57. Xu, X.W.; Mao, Q.; Li, X.H.; Pirajno, F.M.; Qu, X.; Deng, G.; Chen, D.Z.; Zhang, B.L.; Dong, L.H. Copper–zinc albite porphyry in the Hersai porphyry copper deposit, East Junggar, China: A transition between late magmatic and hydrothermal porphyry copper deposit. *Ore Geol. Rev.* **2014**, *61*, 141–156. [CrossRef]
58. Cao, M.J.; Qin, K.Z.; Li, G.M.; Jin, L.Y.; Evans, N.J.; Yang, X.R. Baogutu: An example of reduced porphyry Cu deposit inwestern Junggar. *Ore Geol. Rev.* **2014**, *56*, 159–180. [CrossRef]
59. Richards, J.P. Magmatic to hydrothermal metal fluxes in convergent and collided margins. *Ore Geol. Rev.* **2011**, *40*, 1–26. [CrossRef]
60. Jugo, P.J. Sulfur content at sulfide saturation in oxidized magmas. *Geology* **2009**, *37*, 415–418. [CrossRef]
61. Lee, C.T.A.; Luffi, P.; Chin, E.J.; Bouchet, R.; Dasgupta, R.; Morton, D.M.; Le Roux, V.; Yin, Q.Z.; Jin, D. Copper Systematics in Arc Magmas and Implications for Crust-Mantle Differentiation. *Science* **2012**, *336*, 64–68. [CrossRef]
62. Sun, W.D.; Liang, H.Y.; Ling, M.X.; Zhan, M.Z.; Ding, X.; Zhang, H.; Yang, X.Y.; Li, Y.L.; Ireland, T.R.; Wei, Q.R.; et al. The link between reduced porphyry copper deposits and oxidized magmas. *Geochim. Cosmochim. Ac.* **2013**, *103*, 263–275. [CrossRef]
63. Gartman, A.; Hannington, M.; Jamieson, J.W.; Peterkin, B.; Garbe-Schoenberg, D.; Findlay, A.J.; Fuchs, S.; Kwasnitschka, T. Boiling-induced formation of colloidal gold in black smoker hydrothermal fluids. *Geology* **2018**, *46*, 39–42. [CrossRef]
64. Liu, W.H.; Chen, M.; Yang, Y.; Mei, Y.; Etschmann, B.; Brugger, J.; Johannessen, B. Colloidal gold in sulphur and citrate-bearing hydrothermal fluids: An experimental study. *Ore Geol. Rev.* **2019**, *114*, 103142. [CrossRef]
65. McLeish, D.F.; Williams-Jones, A.E.; Vasyukova, O.V.; Clark, J.R.; Board, W.S. Colloidal transport and flocculation are the cause of the hyperenrichment of gold in nature. *Proc. Natl. Acad. Sci. USA* **2021**, *118*, e2100689118. [CrossRef] [PubMed]
66. Keith, J.D.; Whiney, J.A.; Hattori, K.; Ballantyne, G.H.; Christiansen, E.H.; Barr, D.L.; Cannan, T.M.; Hook, C.J. The role of magmatic sulfides and mafic alkaline magmas in the Bingham and Tintic mining districts, Utah. *J. Petrol.* **1997**, *38*, 1679–1690. [CrossRef]
67. Chen, Y.; Sun, M.X.; Zhang, X.L. SHRIMP U–Pb dating of zircons from quartz at the southeast side of the Baerluke fault, western Junggar, Xinjiang, China. *Geol. Bull. China* **2006**, *25*, 992–994. (In Chinese with English Abstract)
68. Mao, J.W.; Wang, P.A.; Wang, D.H.; Bi, C.S. The tracer of tourmaline for rock-forming and metallogenic environments and its applied conditions. *Geol. Rev.* **1993**, *39*, 497–507. (In Chinese with English Abstract)
69. Sillitoe, R.H.; Sawkins, F.J. Geologic, mineralogic and fluid inclusion studies relating to the origin of copper-bearing tourmaline breccia pipes, Chile. *Econ. Geol.* **1971**, *66*, 1028–1041. [CrossRef]
70. Skewes, M.A.; Holmgren, C.; Stern, C.R. The Donoso copper-rich, tourmaline-bearing breccias pipe in central Chile: Petrologic, fluid inclusion and stable isotope evidence for an origin from magmatic fluid. *Miner. Depos.* **2003**, *38*, 2–21. [CrossRef]
71. Choulet, F.; Faure, M.; Cluzel, D.; Chen, Y.; Lin, W.; Wang, B.; Jahn, B.M. Architecture and evolution of accretionary orogens in the Altaids collage: The early Paleozoic West Junggar (NW China). *Am. J. Sci.* **2013**, *312*, 1098–1145. [CrossRef]
72. Weng, K.; Xu, X.Y.; Ma, Z.P.; Sun, J.M.; Zhang, T. LA-ICP-MS zircon U-Pb geochronology, geochemical characteristics and tectonic significance of Early Devonian volcanic rocks in Malasu area, western Junggar Basin. *Geol. Bull. China* **2015**, *34*, 374–384. (In Chinese with English Abstract)

73. Wu, C. Tectonic Setting and formation mechanism of Reduced Porphyry Copper–Molybdenum Deposit, southern West Junggar. Ph.D. Thesis, China University of Geosciences (Beijing), Beijing, China, 2017. (In Chinese with English Abstract)
74. Rowins, S.M. Reduced porphyry copper-gold deposits: A new variation on an old theme. *Geology* **2000**, *28*, 491–494. [CrossRef]
75. Wu, C.; Liu, Y.; Cao, M.J.; Hong, T.; Xu, X.W.; Dong, L.H. Characteristics and formation mechanism of reduced porphyry Cu and Mo-Cu deposits. *Acta Petrol. Sin.* **2015**, *31*, 617–638. (In Chinese with English Abstract)
76. Hedenquist, J.W.; Lowenstern, J.B. The role of magmas in the formation of hydrothermal ore deposits. *Nature* **1994**, *370*, 519–527. [CrossRef]
77. Cooke, D.R.; Kitto, P.A.; Harris, A.C.; Chang, Z.; Wilkinson, J.J.; Wilkinson, C.C.; Hollings, P.; Webster, J.D. Magma fertility and mineralization. In *Smart Science for Exploration and Mining-Proceedings of the 10th Biennial SGA Meeting*; Economic Geology Research Unit: Townsville, Australia, 2009; Volume 1, pp. 8–10.
78. Xu, W.G.; Zhang, D.H. An interpretation of the role of reduced fluid in prophyry metallogenesis. *Acta Geol. Sin.* **2012**, *86*, 495–502. (In Chinese with English Abstract)

Disclaimer/Publisher's Note: The statements, opinions and data contained in all publications are solely those of the individual author(s) and contributor(s) and not of MDPI and/or the editor(s). MDPI and/or the editor(s) disclaim responsibility for any injury to people or property resulting from any ideas, methods, instructions or products referred to in the content.